ANL-03/3

Practical Superconductor Development for Electrical Power Applications

Annual Report for FY 2002

Argonne National Laboratory, Argonne, Illinois 60439
operated by The University of Chicago
for the United States Department of Energy under Contract W-31-109-Eng-38

Argonne National Laboratory, with facilities in the states of Illinois and Idaho, is owned by the United States Government and operated by The University of Chicago under the provisions of a contract with the U.S. Department of Energy.

Available electronically at http://www.doe.gov/bridge

Available for a processing fee to U.S. Department of Energy and its contractors, in paper, from:

U.S. Department of Energy
Office of Scientific and Technical Information
P.O. Box 62
Oak Ridge, TN 37831-0062
phone: (865) 576-8401
fax: (865) 576-5728
email: reports@adonis.osti.gov

ANL–03/3

ARGONNE NATIONAL LABORATORY
9700 South Cass Avenue
Argonne, Illinois 60439

PRACTICAL SUPERCONDUCTOR DEVELOPMENT FOR ELECTRICAL POWER APPLICATIONS

ANNUAL REPORT FOR FY 2002

U. Balachandran

Contributors:

R. Baurceanu
Y. S. Cha
H. Claus†
S. E. Dorris
J. E. Emerson
R. A. Erck
B. L. Fisher
K. E. Gray†
J. R. Hull
Y. Jee
R. E. Koritala
A. J. Kropf††
M. Li
J. W. Lucas
B. Ma
V. A. Maroni††
R. L. McDaniel
D. J. Miller†
J. J. Picciolo
J. P. Singh
Y. Tang†
B. Veal†
U. Welp†

Energy Technology Division

April 2003

Work supported by

U.S. DEPARTMENT OF ENERGY
Office of Energy Efficiency and Renewable Energy

†Materials Science Division.
††Chemical Technology Division.

Contents

Figures

Tables

PRACTICAL SUPERCONDUCTOR DEVELOPMENT FOR ELECTRICAL POWER APPLICATIONS

ANNUAL REPORT FOR FY 2002

Abstract

Most large-scale applications of high-critical-temperature superconductors will require conductors that can carry large currents in the presence of applied magnetic fields. This report describes progress at Argonne National Laboratory (ANL) in the research and development of practical superconducting components and devices using the Y-Ba-Cu-O and Bi-Pb-Sr-Ca-Cu-O systems. Results are presented in the areas of fabrication of second- and first-generation composite conductors, characterization of their structures and superconducting properties, investigation of grain-boundary current transport and factors that influence it, testing and modeling of the components of a superconducting fault current limiter, and the measurement and modeling of a superconductor's response to a transient such as that in a fault current limiter after a fault.

1 Introduction

The superconductor program at Argonne National Laboratory (ANL) is working to establish the technology that will enable broad-scale commercialization of high-T_c superconductors (HTSs) in a wide variety of electric power applications. The principal objective of this program is to develop methods to fabricate and use structurally reliable HTSs for generation, transmission, and storage of electrical energy. This multifaceted effort seeks to improve the materials properties of HTSs through the understanding and manipulation of processing methods, develop practical methods for mass-producing commercial conductors, fabricate and test prototype conductors, and study basic phenomena in order to understand and predict the performance of HTSs. In this program, the technology and science of fabricating long-length conductors are emphasized. Cooperative relationships with industrial and academic partners are integral to this program. At present, the program focuses on the yttrium-barium-copper oxide and bismuth-lead-strontium-calcium-copper oxide superconductor systems.

Composite and monolithic conductors, in the form of wires, tapes, films, or other shapes, must satisfy several requirements. For most applications, the conductors must be capable of carrying large currents in the presence of large magnetic fields and must be strong, flexible, and chemically and cryogenically stable. Potential applications for such conductors include transmission lines, motors, generators, transformers, magnetic energy storage devices, and electronics. Primary obstacles to the use of bulk HTSs

include low critical current (I_c) and critical current density (J_c) in large applied magnetic fields, relatively poor mechanical properties, and difficulty in efficiently fabricating very long lengths with uniform properties. The ANL HTS program focuses on improving the methods for processing HTSs in order to eliminate each of these obstacles, with the majority of the effort centered on $YBa_2Cu_3O_x$ (YBCO)-coated conductors.

This report reviews the technical progress and status of (1) YBCO tapes fabricated with a variety of architectures; (2) characterization of the microstructures of YBCO-coated conductors; (3) study of factors that influence fundamental grain-boundary properties of YBCO-coated conductors; (4) study of phase development in silver-sheathed $(Bi,Pb)_2Sr_2Ca_2Cu_3O_x$ (Bi-2223) conductors and evaluation of a novel method for processing the Bi-2223 composite conductors; and (5) modeling and testing of key properties of prototype superconducting devices.

2 Technical Progress in 2001-2002

2.1 YBCO-Coated Conductors

2.1.1 Inclined Substrate Deposition (ISD) of MgO Template Layer

ISD is a promising approach for fabricating biaxially textured template layers on nontextured metallic substrates for YBCO-coated conductors. Compared to ion-beam-assisted deposition (IBAD), ISD needs no assisting ion source to develop biaxial alignment and is easier to perform. Unlike the rolling-assisted biaxially textured substrate (RABiTS) approach, which requires complicated high-temperature annealing treatments, ISD yields biaxially textured template films on nontextured metallic substrates at room temperature; consequently, ISD is more robust and less sensitive to heat treatment conditions. Using the ISD approach, biaxially textured template layers have been made from both magnesium oxide (MgO) and yttria-stabilized zirconia (YSZ).

ISD MgO template layers were fabricated on polished Hastelloy C276 (HC) tapes by electron-beam (e-beam) evaporation using an experimental apparatus that is described elsewhere [1]. ISD MgO films consist of columnar grains that stand nearly perpendicular to the substrate surface (Fig. 1a) and are terminated by MgO (002) planes. Because the [002] planes are tilted with respect to the substrate normal, ISD MgO films exhibit a roof-tile structure (Fig. 1b) with a surface roughness of ≈28 nm. To reduce the surface roughness to ≈9 nm, an additional thin (≈0.5 μm) layer of MgO is epitaxially grown at an elevated temperature by e-beam evaporation at a substrate inclination, α, of 0°. Deposition of the homoepitaxial MgO layer also improves the biaxial texture, giving full width at half maximums (FWHMs) of 9.2 and 5.4° for the MgO (002) ϕ- and ω-scans, respectively. Hereafter, unless otherwise indicated, we refer to the template and homoepitaxial MgO layers together as the ISD MgO layer.

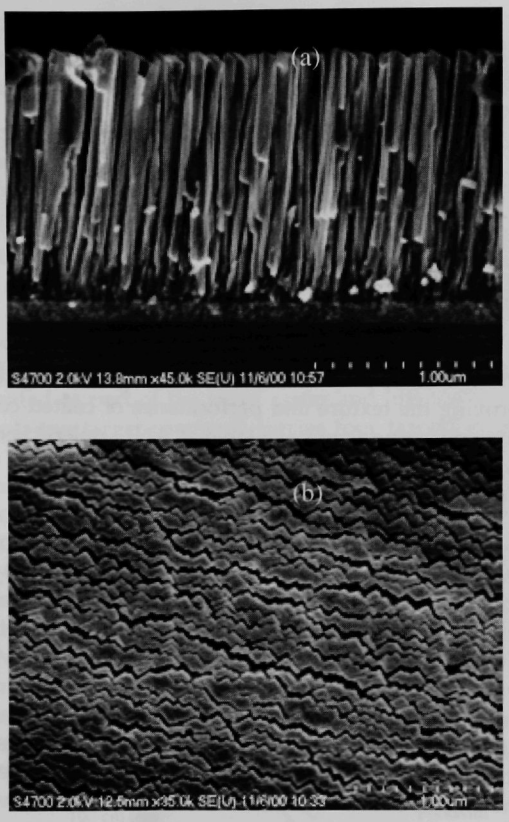

Fig. 1. (a) Cross-sectional and (b) plan-view SEM images of MgO film deposited by ISD using e-beam evaporation.

Because the lattice mismatch between YBCO and MgO is large (≈9%), direct deposition of YBCO on the ISD MgO layer yields poor superconductor properties. After testing of various buffer layers, good superconductor properties were obtained by depositing epitaxial YSZ and CeO_2 layers on the MgO layer before depositing the YBCO layer. The architecture for the ISD MgO approach is illustrated in Fig. 2. YSZ and CeO_2 buffer layers were deposited on ISD MgO films by two techniques. In collaboration with UES, Inc. (Dayton, OH), magnetron sputtering was used to obtain very good biaxial alignment of the YSZ and CeO_2 layers. Los Alamos National Laboratory has reported that magnetron sputtering also gives good biaxial alignment of

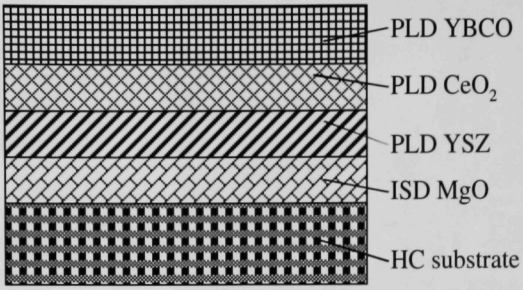

Fig. 2.
Layer structure of YBCO deposited on HC substrates by the ISD approach.

YSZ and CeO_2 on MgO films prepared by IBAD. Magnetron sputtering clearly offers potential for improving the texture and performance of coated conductors; however, because magnetron sputtering is not available at ANL, pulsed laser deposition (PLD) was used to grow YSZ and CeO_2 buffer layers on ISD MgO films. The conditions that were used to grow the buffer layers are listed in Table 1.

Mechanically polished HC coupons (≈0.1 mm x ≈5 mm x 1 cm) were used as the substrates for deposition of ISD MgO templates, YSZ and CeO_2 buffer layers, and YBCO films. A root-mean-square (RMS) surface roughness of 2-3 nm was measured by atomic force microscopy (AFM) on HC substrates that were polished with 0.25 μm diamond paste. To evaluate the effect of surface roughness, we also polished HC substrates with various coarser grinding media to obtain surface roughnesses ranging up to 15 nm. Fused lumps of MgO (Alfa Aesar, 99.95% metals basis, 3-12 mm pieces) were used as the target material for growing MgO films. Substrates were mounted on a sample stage that can be tilted above the e-beam evaporator to give a range of substrate inclinations, α, the angle between the substrate normal and the evaporation direction.

Table 1. Conditions used for epitaxial growth of YSZ and CeO_2 buffer layers by PLD

Laser wavelength	248 nm (Kr-F)
Repetition rate	2-8 Hz
Pulse width	25 ns
Energy density	1-3 J/cm^2
Substrate temperature	700-800°C
Operating pressure	1-100 mtorr
Oxygen flow rate	1-10 sccm
Target-to-substrate distance	4-8 cm

In this study, α was ≈55°. High purity oxygen flowed into the system at ≈3 sccm during film deposition. The base pressure was 1×10^{-7} torr and rose to ≈2×10^{-5} torr during deposition. A quartz crystal monitor beside the sample stage monitored and controlled the deposition rate. Deposition rates of 20-100 Å/sec were used, and the substrate temperature during deposition was maintained between room temperature and 50°C. After deposition of the ISD films, a dense, thin, homoepitaxial layer of MgO was deposited at elevated temperature (≈700°C) and α ≈0°.

Buffer layers and YBCO films were deposited using PLD2, a PLD system that was designed and constructed during FY 2002 and was described previously [2]; it is shown schematically in Fig. 3. PLD2 uses an optical beam raster to produce films with better uniformity over a broader area. Its laser beam is focused at the target through a quartz lens (1000 mm focal length) that has an anti-reflective coating. The beam is reflected by a mirror that is mounted as part of the beam raster and hits the target at an incident angle of 45°. The rotating target carrousel carries four targets to accommodate the ablation of multiple layers without breaking vacuum. Commercial targets (99.999% pure, 45 mm in diameter x 6 mm thick) from Superconductive Components were used. Substrates were attached to a heated sample stage with silver paste and heated to 700-800°C during deposition. The base pressure of the PLD chamber was ≈1×10^{-5} torr. An operating pressure of 100-300 mtorr was maintained by flowing ultra-high-purity oxygen at ≈10 sccm and pumping the chamber with a molecular turbo pump. The spot size of the laser beam on the rotating target had an area of ≈12 mm^2, which gave an energy density of ≈2.0 J/cm^2. The distance between the target and the substrates was ≈7 cm.

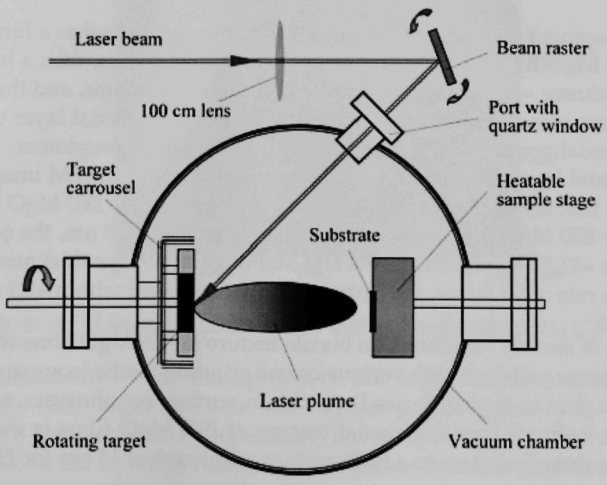

Fig. 3. Schematic illustration of PLD system.

The superconducting critical transition temperature (T_c) and critical current density (J_c) were determined by the inductive method in which superconductor samples are placed between a primary and a secondary coil, each with an inner diameter of ≈1 mm and an outer diameter of ≈5 mm. An alternating current of 1 kHz is introduced into the primary coil and detected by the secondary coil using a lock-in amplifier (Stanford Research Systems SR830 DSP). The transport J_c of selected samples was measured by the four-point method at 77 K in liquid nitrogen. The electric field criterion was 1 μV/cm. Samples for the transport measurements were first coated with 2-μm-thick silver by e-beam evaporation and then annealed in flowing high-purity oxygen at 400°C for 2 h.

Film textures were characterized by X-ray diffraction (XRD) pole figure analysis using Cu-K_α radiation. The in-plane textures of ISD MgO films and subsequently deposited buffer layers were characterized by the FWHMs of φ-scans for the (002) reflections, and the out-of-plane textures were characterized by the FWHM of ω-scans at the [001] pole for the same reflection. The in-plane texture of YBCO was measured by the FWHM of the YBCO(103) φ-scan, and the out-of-plane texture was measured by the FWHM of the YBCO(005) ω-scan. The surface morphology of individual layers was examined using a Hitachi S-4700-II scanning electron microscope (SEM), and selected area diffraction (SAD) with a Philips CM30 transmission electron microscope (TEM) was used to derive the crystalline orientation relationships among the ISD MgO template, YSZ and CeO_2 buffer, and YBCO films. Surface roughness was measured in the tapping mode using a Digital Instruments Dimension 3100 SPM Atomic Force Microscope (AFM).

The development of biaxial texture in MgO films was studied as a function of film thickness. ISD MgO films were grown with various thicknesses, then a homoepitaxial MgO layer (thickness ≈ 0.5 μm) was deposited on each of the films, and the FWHM of a MgO (002) φ-scan was measured for each film. The homoepitaxial layer was added to sharpen the biaxial texture of the film and reduce its surface roughness. The effect of the homoepitaxial layer on surface roughness is shown in the AFM images of Fig. 4. Figure 5 shows that the in-plane texture quickly improves as the ISD MgO layer is made thicker. As the ISD MgO film thickness increases from 0.1 to 0.5 μm, the φ-scan FWHM decreases from ≈21.5° to ≈10.5°; the FWHM stabilizes at ≈9° for thickness of >0.5 μm. At a deposition rate of 50 Å/sec, the texture is fully developed within ≈1.5 min.

The effect of surface roughness on biaxial texture in ISD MgO films was evaluated. HC substrates were polished with various coarse grinding media (compared to 0.25-μm diamond paste that is typically used) to obtain surface roughnesses ranging up to 15 nm. Figure 6 shows that the biaxial texture of ISD MgO films is independent of substrate surface roughness up to a RMS surface roughness of 15 nm for ISD MgO films of ≈2 μm thickness.

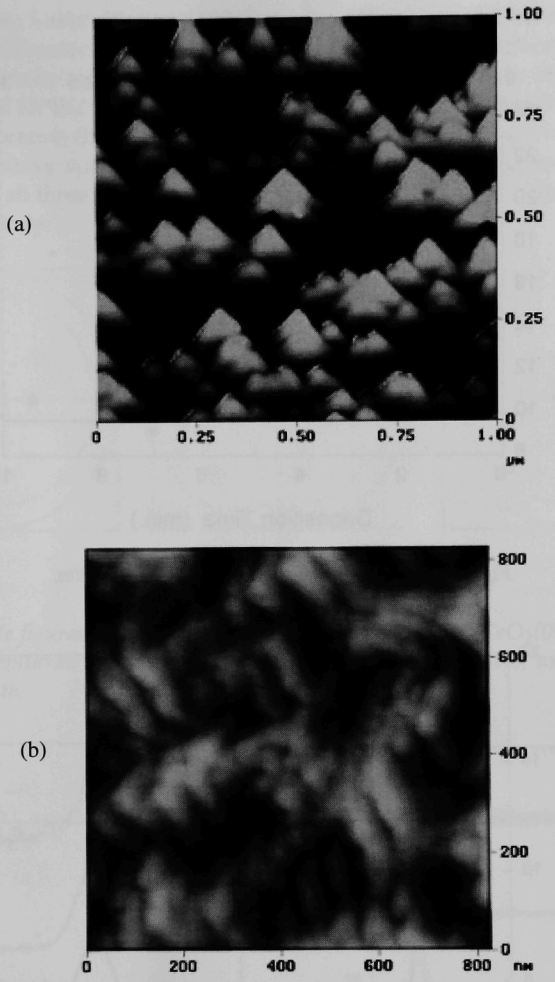

Fig. 4. AFM images of (a) ISD MgO and (b) homoepitaxial MgO films.

The biaxial texture of YSZ films grown on ISD MgO templates can be significantly affected by the laser repetition rate and oxygen partial pressure in the deposition chamber. For a given substrate temperature, lower repetition rate and reduced oxygen partial pressure in the chamber both help to improve epitaxial growth of the YSZ film. However, a lower repetition rate requires longer deposition time to produce a film with

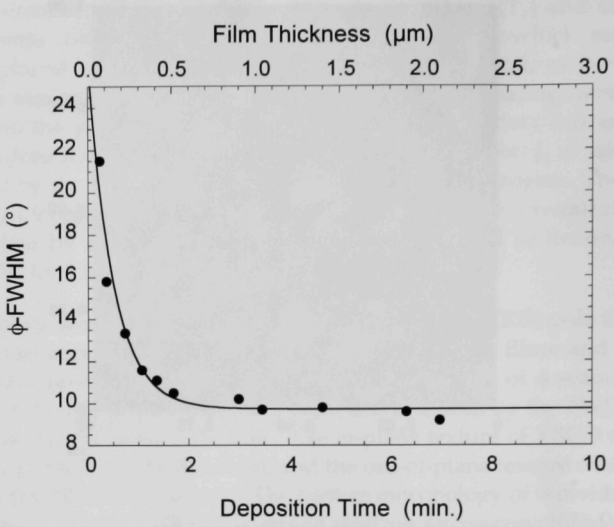

Fig. 5. Texture development in the ISD MgO film.

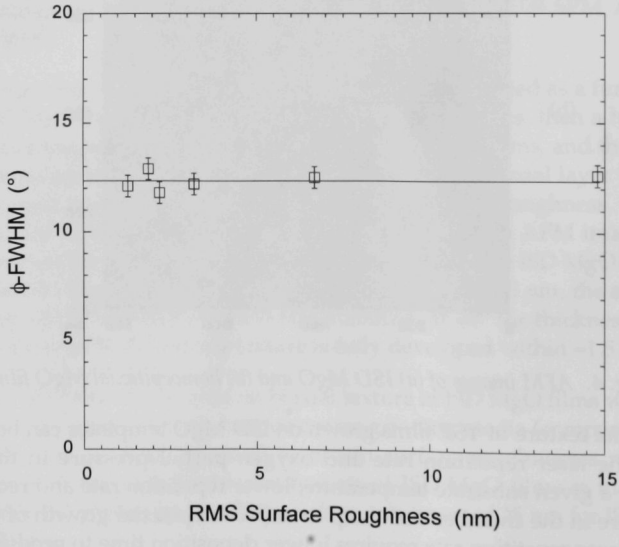

Fig. 6. In-plane texture as a function of substrate surface roughness for ISD MgO films of 2-μm thickness.

a given thickness. Laser ablation of YSZ at a repetition rate of 2 Hz onto an ISD MgO film at 800°C in ≈20 mtorr oxygen resulted in good epitaxial growth of the YSZ. Similar conditions can also be used to grow CeO_2 films with good epitaxy. Figure 7 shows the (002) pole figures for the MgO, YSZ, and CeO_2 layers, where the MgO layer was grown by e-beam evaporation (ISD), and the YSZ and CeO_2 layers were grown by PLD. Good cube-on-cube epitaxy was obtained in both the YSZ and CeO_2 layers. The (002) and (220) ϕ-scans for all three layers are shown in Fig. 8; the FWHMs for the scans were ≈12° and 16°, respectively.

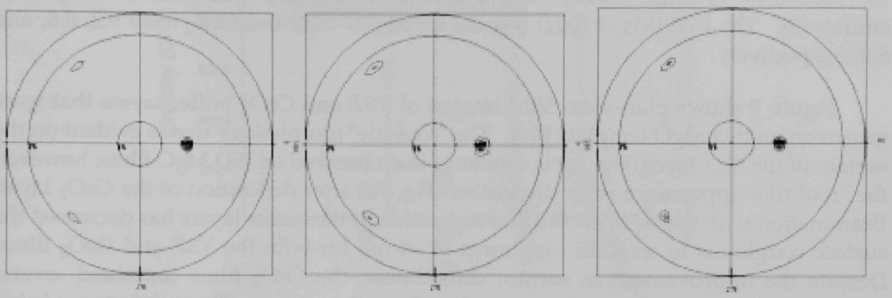

(a) (b) (c)

Fig. 7. X-ray pole figures for (a) MgO(002), (b) YSZ(002), and (c) CeO_2(002), showing cube-on-cube epitaxial relationship among CeO_2, YSZ buffer layers, and ISD MgO film underneath.

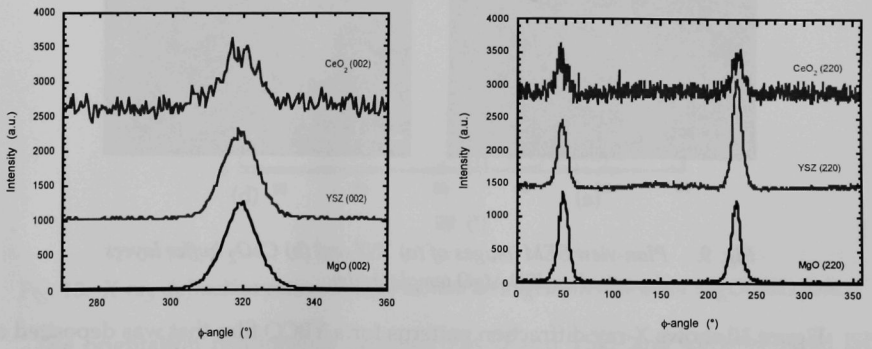

(a) (b)

Fig. 8. Patterns from (a) (002) and (b) (220) ϕ-scans for MgO grown by e-beam evaporation (ISD), and YSZ and CeO_2 grown by PLD.

YSZ and CeO_2 films were epitaxially grown on top of ISD MgO films by PLD using the conditions listed in Table 1. The layer thicknesses for YSZ and CeO_2 were ≈200 nm and ≈10 nm, respectively. The CeO_2 and YSZ layers both showed a cube-on-cube epitaxial relationship with the ISD MgO template film. Figure 7 shows (002) pole figures for the MgO, YSZ, and CeO_2 layers. These show that the c-axes for the YSZ and CeO_2 buffer films are both tilted at the same angle (≈32°) as the ISD MgO template film, and they suggest a cube-on-cube epitaxial relationship in which CeO_2<100> // YSZ<100> // MgO<100> and CeO_2<010> // YSZ<010> // MgO<010> or CeO_2<001> // YSZ<001> // MgO<001>. This epitaxial relationship was confirmed by TEM studies [3]. The FWHMs of (002) ϕ-scans for MgO, YSZ, and CeO_2 were 9.2, 8.8, and 8.0°, respectively.

Figure 9 shows plan-view SEM images of YSZ and CeO_2 buffer layers that were grown on an ISD MgO template film. The "roof-tile" morphology that is evident on the surface of the YSZ layer (Fig. 9a) is similar to that observed on ISD MgO films; however, the "roof tile" appearance is hardly visible (Fig. 9b) after deposition of the CeO_2 layer. Examination with the AFM shows that deposition of the buffer layers has decreased the surface roughness to an RMS roughness of ≈8 nm for both the YSZ and CeO_2 films. Despite the improvement in surface smoothness, the CeO_2 films contained several defects such as pits and particles protruding from the surface. These defects are being further studied to determine their influence on the superconductor properties of a YBCO film that is deposited on top of it.

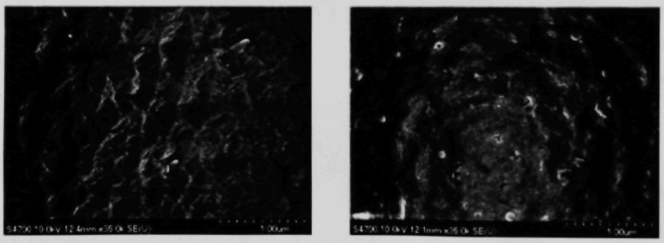

(a) (b)

Fig. 9. Plan-view SEM images of (a) YSZ and (b) CeO_2 buffer layers deposited on ISD MgO template film.

Figure 10 shows X-ray diffraction patterns for a YBCO film that was deposited on a YSZ-and CeO_2-buffered ISD MgO substrate. The patterns were collected in the two sample orientations that are indicated by insets in the patterns. In the normal orientation (Fig. 10a), only YBCO (00*l*) peaks are seen, which indicates that the c-axis of YBCO is parallel to the substrate normal. No diffraction peaks are observed for MgO, YSZ, or CeO_2 in this orientation, because these layers are tilted with respect to the

substrate normal and the Bragg diffraction condition is not satisfied. In the tilted orientation (Fig. 10b), the sample is rotated to observe the MgO(002) reflection. In this orientation, the (002) reflections for YSZ and CeO_2 are also observed, indicating that they have the same orientation as MgO, whereas the (00*l*) peaks of YBCO are absent.

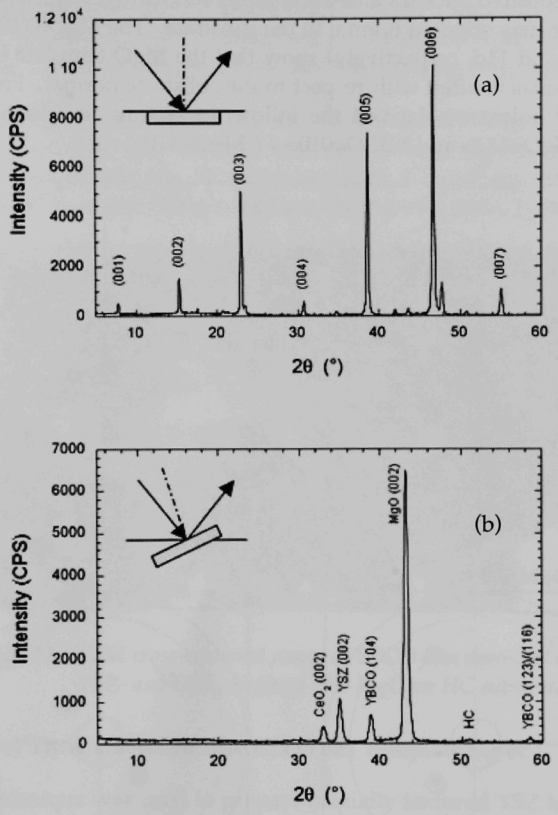

Fig. 10. X-ray diffraction patterns (a) at normal arrangement and (b) at MgO(002) pole.

The orientation relationship between YBCO and YSZ- and CeO_2-buffered ISD MgO was analyzed. Because CeO_2 has a very close lattice match with the YBCO pseudo-cell and the YBCO unit cell is larger than that of CeO_2, the X-ray diffraction peaks for YBCO overlap those of CeO_2. For this reason, the crystalline texture of CeO_2 is difficult to analyze after YBCO has been deposited. However, because the YSZ and CeO_2 buffer layers grow epitaxially on MgO, their orientation relationship with YBCO

should be equivalent to that between YBCO and the MgO template layer, assuming that the orientations of YSZ and CeO_2 do not change during the deposition of YBCO.

The YBCO(005) pole figure (Fig. 11a) shows a single pole at its center, while the YBCO(103) pole figure has four evenly distributed poles (Fig. 11b). This confirms that the YBCO films deposited on YSZ- and CeO_2-buffered ISD MgO substrates are biaxially textured with the c-axis oriented normal to the substrate. The MgO(002) and (220) pole figures (Figs. 11c and 11d, respectively) show that the MgO template is also biaxially textured, but its c-axis is tilted with respect to the substrate normal. From the relative positions of their poles, we derived the following unique orientation relationship: YBCO<100> // MgO<111> and YBCO<010> // MgO<110>.

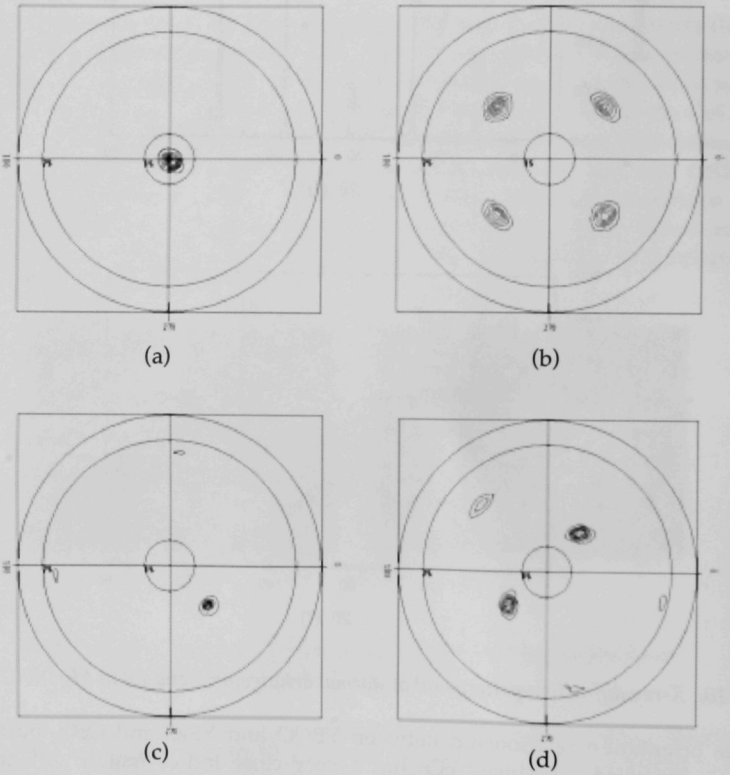

Fig. 11. X-ray pole figures for (a) YBCO(005), (b) YBCO(103), (c) MgO(002), and (d) MgO(220) measured on the same sample.

The orientation relationship between YBCO and YSZ- and CeO_2-buffered ISD MgO was confirmed by TEM. Figure 12 shows a cross-sectional image of YBCO on YSZ- and CeO_2-buffered ISD MgO on HC; Fig. 13 shows results from selected area diffraction along the [111] zone axis for MgO and YSZ. These results confirm the relationship that was derived from the pole figures, but this relationship differs from the one that was reported earlier [4] where YBCO<001> // MgO<001> and YBCO<100> // MgO<100>. We believe that the difference in orientation relationship resulted from differences in the YBCO growth conditions and the buffer layer architecture.

YBCO coated conductors that were fabricated with the ISD MgO architecture (with c-axis of YBCO normal to the substrate) exhibited a sharp superconducting transition with T_c = 91 K. As shown in Fig. 14, a transport J_c of 5.5×10^5 A/cm^2 was measured at 77 K in self-field on a sample that was 0.46-μm thick, 4-mm wide, 1-cm long.

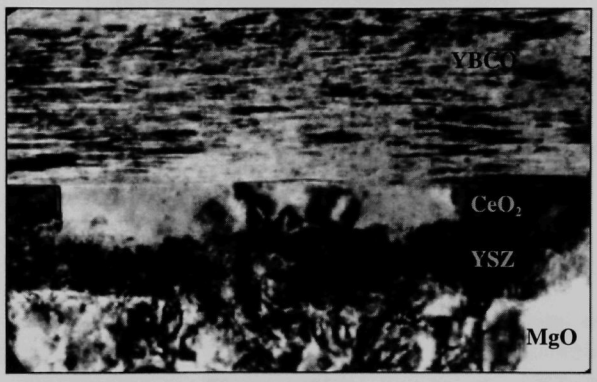

Fig. 12. TEM cross-sectional image of YBCO film deposited on YSZ- and CeO_2-buffered ISD MgO on HC substrate.

2.1.2 ISD of Yttria-stabilized Zirconia (YSZ) Template Layer

The ISD technique was used to prepare biaxially textured YSZ template layers on untextured HC and silicon (Si) substrates. This process may be simpler and faster than the ISD MgO process, because it eliminates the need for ISD-MgO and homoepitaxial MgO layers. We describe here results from a preliminary survey of the ISD conditions for obtaining biaxially textured YSZ films on untextured substrates.

Figure 15 shows a schematic of the equipment that was used for ISD of YSZ template layers on HC substrates. Unlike ISD MgO films that are deposited by electron beam evaporation, ISD YSZ films are deposited using a Lambda Physik LPX-210i excimer laser system. Polished HC substrates were mounted on a tiltable heater with

silver paste. The substrate inclination, α, defined as the angle between the substrate normal and the direction of the laser plume, was varied in the range of 45-55°. Within this range, α did not significantly affect the texture of the films. In this report, the typical value for α was 50°. Both HC and Si wafers were used as substrates for ISD YSZ films. X-ray diffraction results showed that the type of substrate had little effect on the orientation and biaxial texture of YSZ films; however, to obtain similar orientation and texture in the YSZ films, the substrate temperature (T_s) had to be ≈30°C higher for films grown on Si substrates. This difference in T_s may result from a difference in the actual surface temperature for the same nominal T_s. Details of the experimental parameters are listed in Table 2.

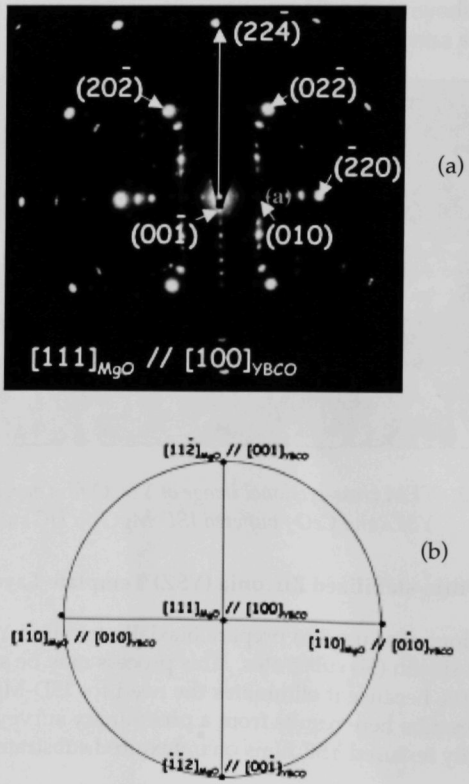

Fig. 13. (a) TEM selected area diffraction along MgO [111] zone axis, and (b) a stereographic projection showing orientation relationship between YBCO and MgO films.

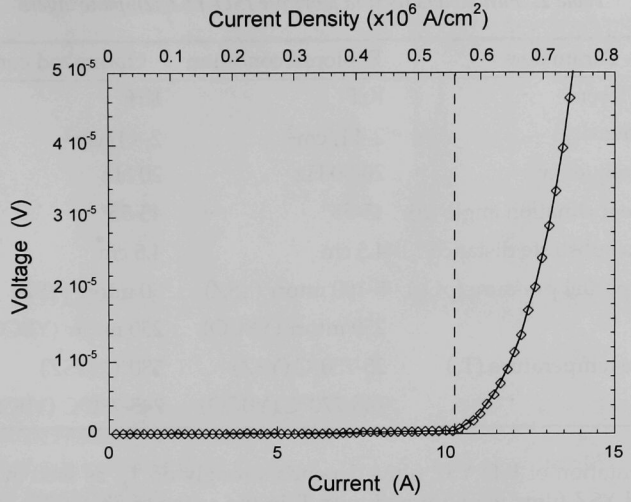

Fig. 14. Transport J_c of YBCO on ISD MgO measured at 77 K in self-field.

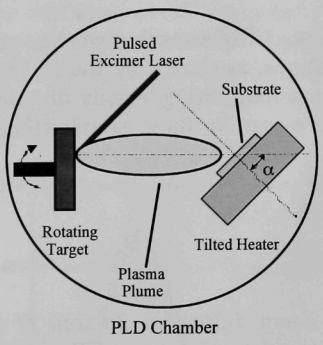

Fig. 15.
Schematic of the arrangement used for inclined substrate deposition of YSZ template layers on HC substrates by pulsed laser deposition (PLD).

Important factors in obtaining (001)-oriented YSZ films, i.e., films whose (001) planes are parallel to the substrate surface, include T_s and oxygen partial pressure, pO_2. In the present study, T_s was varied from 25-750°C, and pO_2 ranged from 100 mtorr. ISD YSZ films were grown with thickness in the range 0.5-2.5 μm. As the thickness increased, the biaxial alignment improved as seen by a decrease in the FWHM for YSZ(111) ϕ-scans. The best biaxial alignment was obtained with pO_2 = 50 mtorr and thickness ≥2.0 μm, giving FWHM of 16°.

Table 2. Parameters used to fabricate ISD YSZ template layers

Parameters	Explored condition	Optimized condition
Excimer laser	KrF	KrF
Energy density	2-4 J/cm^2	2-4 J/cm^2
Repeat frequency	20-50 Hz	20 Hz
Substrate inclination angle (α)	45-55°	45-55°
Target-to-substrate distance	4.5 cm	4.5 cm
Oxygen partial pressure (pO_2)	5-100 mtorr (YSZ)	50 mtorr (YSZ)
	250 mtorr (YBCO)	250 mtorr (YBCO)
Substrate temperature (T_s)	25-750°C (YSZ)	580°C (YSZ)
	745-770°C (YBCO)	745-770°C (YBCO)

The orientation of ISD YSZ films depends strongly on T_s, as seen in Fig. 16. The (111)-oriented YSZ films were formed with T_s in the range of 25-400°C. When T_s was increased to 550-600°C, the YSZ films contained only (002)-oriented grains. Increasing T_s above 650°C, a mixed orientation, with both (111)- and (002)-oriented grains being evident.

Good biaxial texture was observed in (001)-oriented YSZ films that were prepared under the optimized T_s and pO_2 deposition conditions, as shown by the (111) pole figure (Fig. 17) for one such film. This pattern shows four strong, evenly distributed peaks with a chi-angle of 54.7°. A typical YSZ(111) ϕ-scan for these samples (Fig. 18)

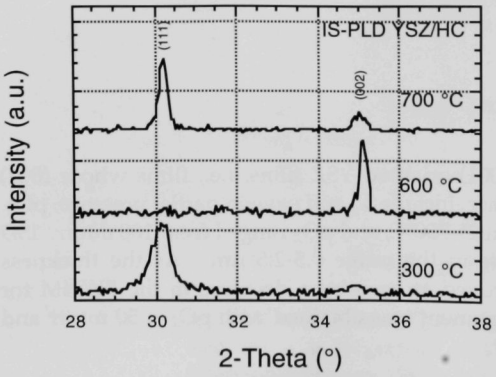

Fig. 16.
X-ray diffraction 2θ-scan of YSZ template layers on HC substrates made by inclined substrate deposition using pulsed laser deposition at different T_s.

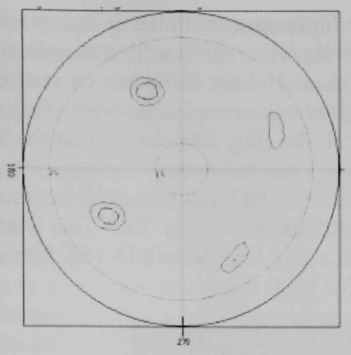

Fig. 17. YSZ(111) pole figure of YSZ grown on Hastelloy C substrate by inclined substrate deposition using pulsed laser deposition.

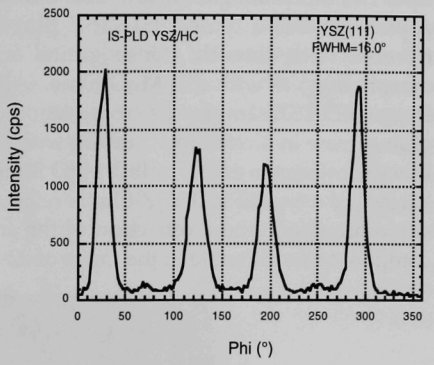

Fig. 18. YSZ(111) ϕ-scan of YSZ grown on Hastelloy C substrate by inclined substrate deposition using pulsed laser deposition.

shows four strong, sharp peaks and gives an FWHM of 16.0°. These results indicate good biaxial texture with YSZ(002) planes oriented parallel to the substrate. An Ω-scan for the (002) pole of (001)-oriented YSZ (Fig. 19) gave an FWHM value of 7.6°, indicating a small dispersion in the out-of-plane orientation. The tilt angle of YSZ(002), defined as the angle between the normal to the (002) planes and the normal to the substrate, varied between 0 and 15°. The cause for this variation in tilt angle is being further investigated.

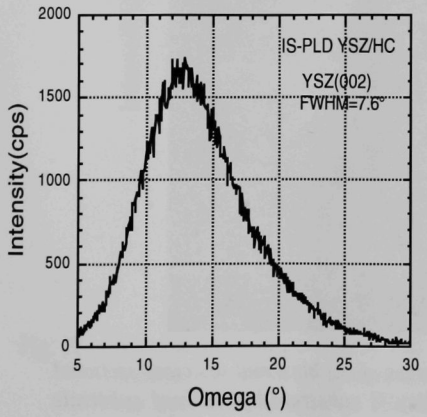

Fig. 19. YSZ(002) Ω-scan of YSZ grown on Hastelloy C substrate by inclined substrate deposition using pulsed laser deposition.

The morphologies of ISD YSZ and ISD MgO films appear similar in many ways. A plan-view of a typical ISD YSZ film (Fig. 20a) shows a surface that is uniformly covered with smooth, dense grains arranged in a slightly terraced, or roof-tile, morphology, as with ISD MgO films. Although tilted columnar grains were observed in one ISD YSZ sample, the cross section of a typical film (Fig. 20b) shows that the YSZ grains grow in a columnar fashion with the columns oriented normal to the substrate, like the columnar grains of ISD MgO films. Compared to ISD MgO films, however, the surface of a typical ISD YSZ film is relatively smooth, as seen in Fig. 20b. This relative smoothness may be a reflection of the smaller tilt angle (≤15°) for ISD YSZ films, as compared to a tilt angle in the range of 22-32° for ISD MgO films.

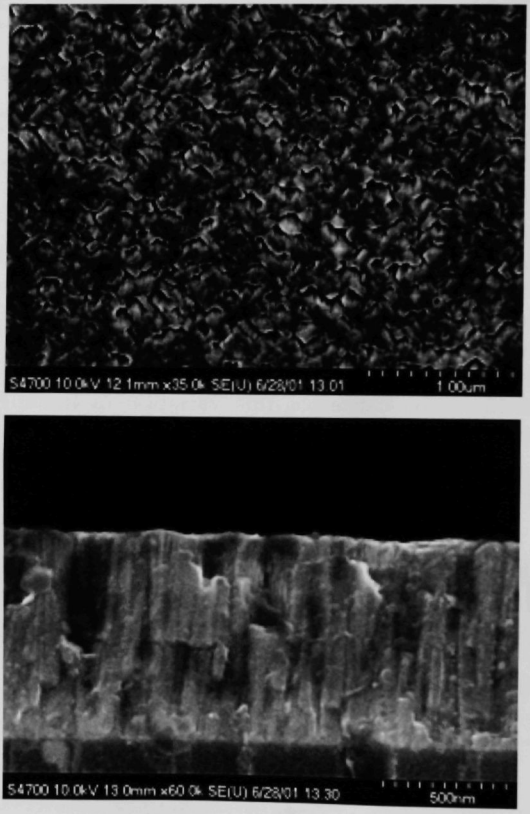

Fig. 20. Scanning electron microscope images of (a) plan and (b) cross-sectional views of YSZ grown on Hastelloy C substrate by inclined substrate deposition using pulsed laser deposition.

Using normal PLD geometry, i.e., with a substrate inclination of 0°, YBCO films were deposited on ISD YSZ layers that had been grown on HC substrates. The thickness of the YBCO films was ≈0.5 μm. A thin layer of CeO_2 was deposited on the YSZ prior to YBCO deposition to decrease the lattice mismatch with YBCO. For some samples, an extra homoepitaxial YSZ layer was grown on top of the ISD YSZ template layer. A typical X-ray diffraction 2θ-scan from one of these films (Fig. 21) shows greatly dominant (00l) peaks for YBCO, indicating that the c-axis of YBCO grains is oriented normal to the substrate. The YBCO(005) and (103) pole figures are shown in Fig. 22. The (103) pole figure shows four strong, evenly distributed peaks, indicating that the film is biaxially textured. A YBCO(103) φ-scan (Fig. 23) gave an FWHM of 18.4°, indicating good in-plane alignment in the film. The superconducting transition for one of the films (Fig. 24) had a T_c(onset) of 89.5 K with a ΔT_c of ≈4 K. J_c for the films is in the range of 1.0-1.5 x 10^5 A/cm^2.

2.1.3 Direct Deposition of YBCO on Ag

YBCO films were deposited directly on polycrystalline silver (Ag) substrates by inclined substrate PLD [1]. This method has the potential to simplify fabrication of coated conductors by eliminating the need for multiple buffer layers. Examination of YBCO films on Ag that contained 350 ppm copper (Cu) showed (Fig. 25a) that they

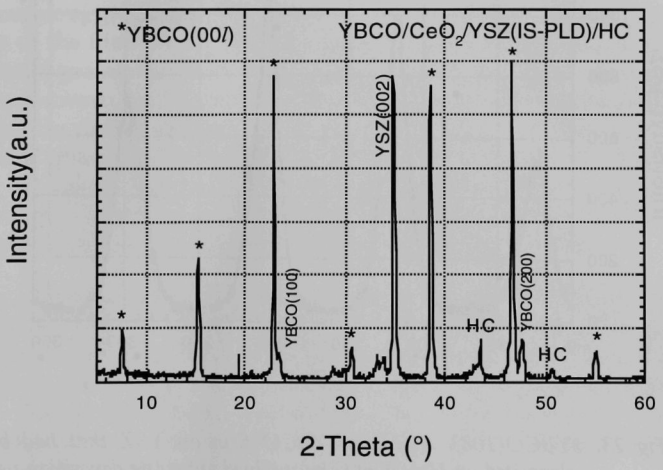

Fig. 21. X-ray diffraction 2θ-scan of YBCO on YSZ that had been deposited on Hastelloy C substrate by inclined substrate deposition using pulsed laser deposition. A CeO_2 cap layer was deposited on YSZ before deposition of YBCO.

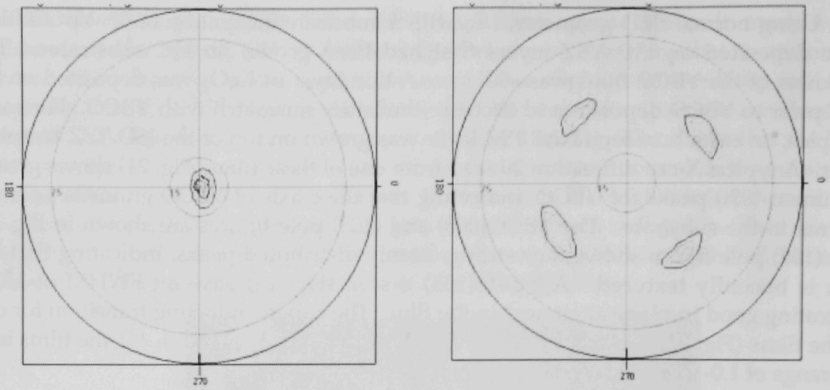

Fig. 22. (a) YBCO(005) and (b) YBCO(103) pole figures of YBCO on YSZ that had been deposited on Hastelloy C by inclined substrate deposition using pulsed laser deposition.

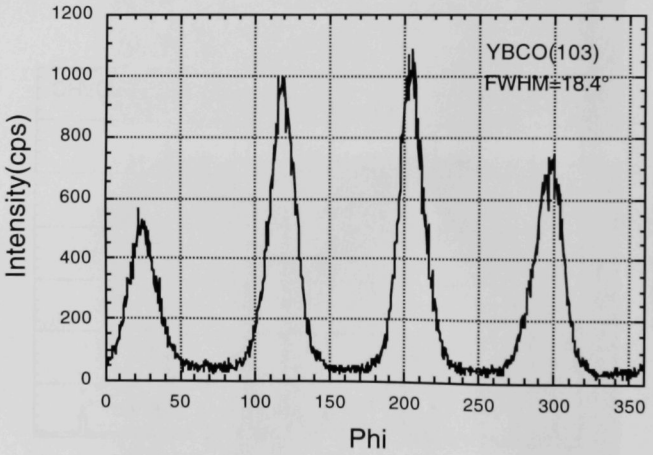

Fig. 23. YBCO(103) ϕ-scan of YBCO film on YSZ that had been deposited on Hastelloy C by inclined substrate deposition using pulsed laser deposition.

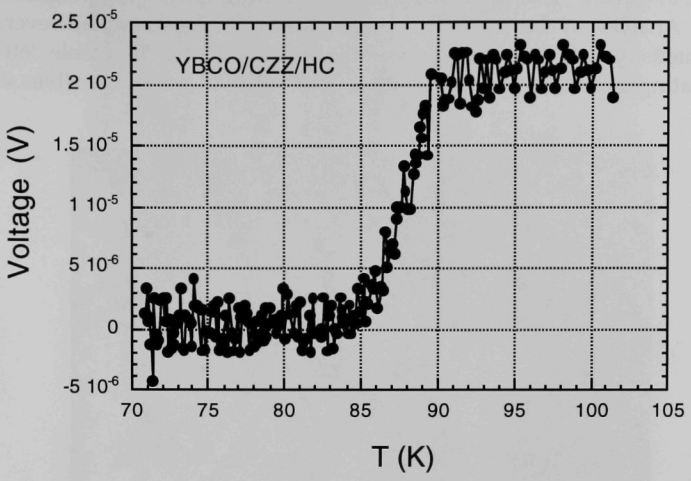

Fig. 24. Inductively measured superconducting transition for YBCO on YSZ that had been deposited on Hastelloy C by inclined substrate deposition using pulsed laser deposition.

contain a mosaic of irregularly shaped areas with clear sharp boundaries between them. In all areas of the film, there were short (≈0.5 μm) rectangular grains that resembled a-axis oriented grains; however, the orientation of these grains was not confirmed. A boundary between two areas of the film, seen in Fig. 25b at higher magnification, showed that the darker area appeared denser and contained relatively few "a-axis" grains. The brighter area seemed less dense and had a higher concentration of "a-axis" grains, all apparently oriented in a particular direction. It is not known how the in-plane texture varies between the various areas. Energy dispersed x-ray analysis in the SEM showed no obvious composition difference among the areas.

The morphology of the YBCO film appeared to be directly related to that of the silver substrate. This relationship was seen by comparing the morphology of a YBCO film (Fig. 26a) to that of its silver substrate after removal of the YBCO film (Fig. 26b). Both images show twinning, and in many cases there is direct correspondence between the images. The similarity in size and shape of the grains clearly shows the correlation in morphology between YBCO and silver, and suggests that the microstructure of the YBCO film was influenced by that of the silver substrate.

The XRD pattern of the YBCO film on polycrystalline silver (Fig. 27) consists of sharp and strong peaks, all of which were identified as YBCO(00*l*) peaks. No peaks associated with a-axis orientation appear in this pattern. An Ω-scan of the YBCO(005)

peak (Fig. 27b) gave an FWHM value of 3.8°, indicating good c-axis alignment of the YBCO film. Analysis of the YBCO(103) pole figure (Fig. 27c) shows, however, that the diffracted intensity is more-or-less uniformly distributed over the whole 360° ϕ-angle range, indicating a random in-plane texture. The XRD pattern for the silver substrates

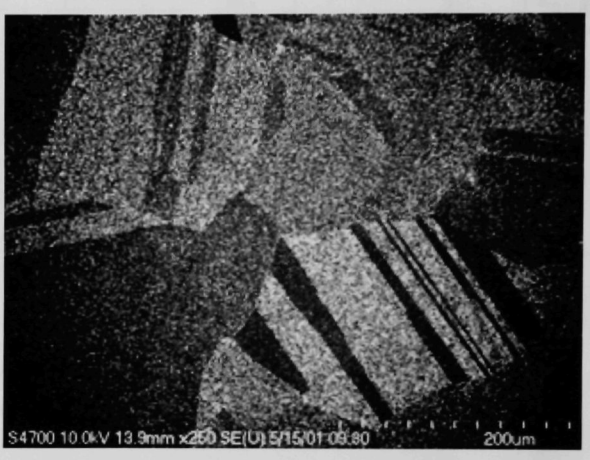

(a)

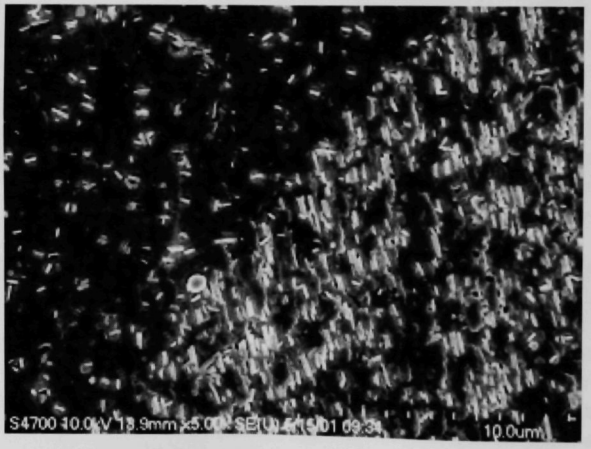

(b)

Fig. 25. Secondary electron images of YBCO films on silver showing sharp borders between different regions of the film.

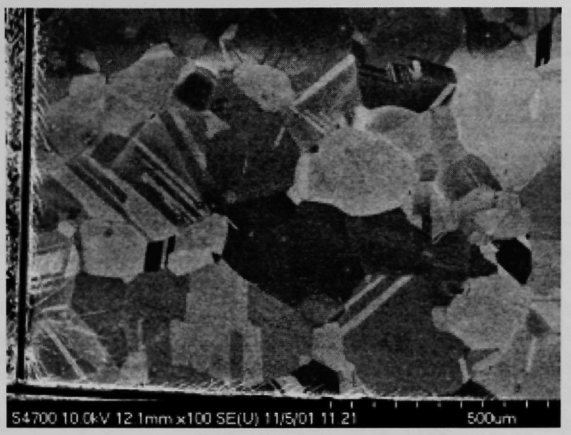

(a)

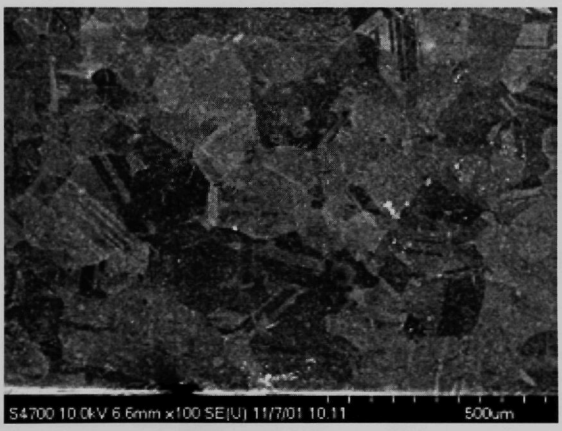

(b)

Fig. 26. SEM images of (a) YBCO film and (b) Ag substrate at the same area after YBCO film was removed from the substrate. Morphology correlation between them can be seen clearly.

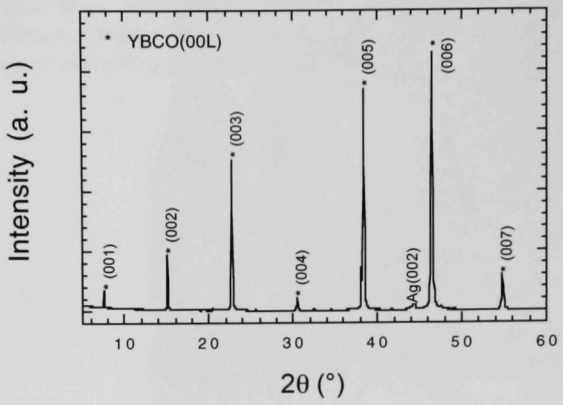

(a)

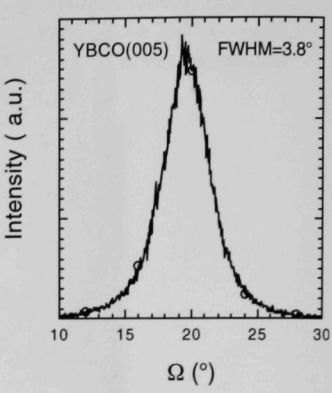

(b)

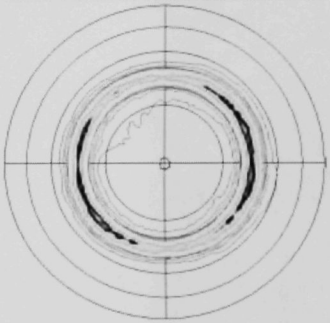

(c)

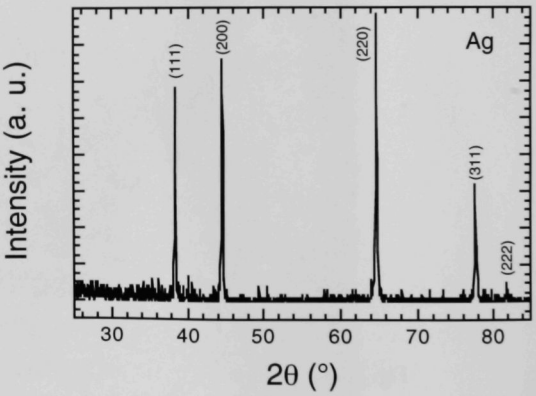

(d)

Fig. 27. X-ray diffraction patterns of YBCO/Ag films: (a) 2θ-scan, (b) Ω-scan of YBCO(005), (c) pole-figure of YBCO(103), and (d) 2θ-scan of Ag substrates.

(Fig. 27d) shows roughly equivalent intensities for the (111), (200), (220), and (311) diffraction peaks, indicating that the substrate shows no preferred orientation. Ω-scans for each of these peaks gave a wide distribution of intensity (FWHM=10~15°), suggesting a highly random orientation of the silver grains.

Raman spectra were also used to obtain information about microstructure, cation disorder, and second-phase formation such as CuO and $BaCuO_2$. Figure 28 shows the Raman spectrum of typical as-grown YBCO films, which exhibit a strong Raman band at 340 cm^{-1}, along with a weak band centered at about 500 cm^{-1}. The spectrum was recorded in the xx/yy mode, in which the laser excitation and observation directions were perpendicular to the substrate. In this configuration, a stoichiometric YBCO film with perfect c-axis orientation should exhibit only one band at ≈340 cm^{-1} over the range of 200 to 800 cm^{-1}. The existence of the weak band at around 500 cm^{-1} may indicate some degree of c-axis misalignment in the YBCO film [5-6], but may also be attributed somewhat to a lack of in-plane texture. The absence of other peaks suggests that the YBCO film has a stoichiometric composition.

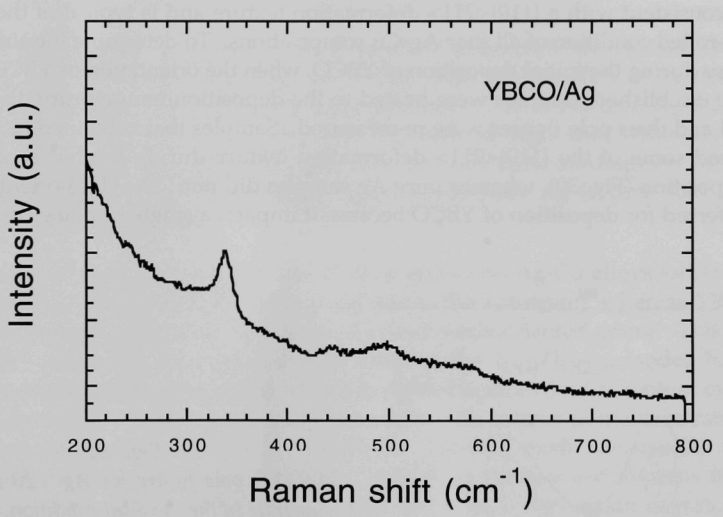

Fig. 28. Raman spectrum of YBCO films grown on polycrystalline Ag substrates.

TEM examinations of YBCO on untextured Ag showed that the YBCO films were in fact slightly Cu deficient [1], suggesting that Cu had diffused into the Ag substrate during YBCO deposition. This motivated an investigation of Ag-Cu alloys as substrates for YBCO deposition in an effort to reduce the driving force for Cu diffusion. For this study, YBCO films were prepared by PLD on Ag substrates that contained various

amounts of Cu (9 ppm by weight, subsequently called "pure" Ag, and 0.15, 0.2, and 0.25 at.% Cu). The YBCO films were characterized by their Raman spectra, X-ray pole figures, T_c and J_c, and the results were correlated with the Cu content of the substrate.

The Ag-Cu alloys used in this work were prepared by a vacuum melt process followed by cold-rolling in air at room temperature. The total reduction ratio was >95% with 5% deformation per pass. No recrystallization heat treatment was given to the samples prior to the deposition of YBCO. Next, YBCO films (thickness = 0.5 μm) were deposited using a KrF excimer laser on small pieces (10 x 5 mm^2) cut from these Ag-Cu strips. The YBCO films were deposited at 770°C with 290 mtorr oxygen background pressure, at a repetition rate of 8 Hz and an energy density of 1.1 J/cm^2. The T_c and J_c of the films were measured by an inductive method. The out-of-plane texture, presence of impurity phases, and cation disorder in the films were determined by Raman spectroscopy; and in-plane texture development was evaluated by XRD pole figure analysis.

Figure 29 shows the (111) pole figure for the as-rolled sample with 0.20 at.% Cu, which is consistent with a {110}<211> deformation texture and is typical of the results for the as-rolled condition of all four Ag-Cu compositions. To determine the stability of this texture during the initial deposition of YBCO, when the orientation of YBCO grains should be established, samples were heated to the deposition temperature, then were quenched and their pole figures were re-measured. Samples that contained (≥0.15 at.% Cu retained some of the {110}<211> deformation texture during the initial stages of YBCO deposition (Fig. 30), whereas pure Ag samples did not. The (110)-orientation of Ag is preferred for deposition of YBCO because it imparts a single in-plane orientation

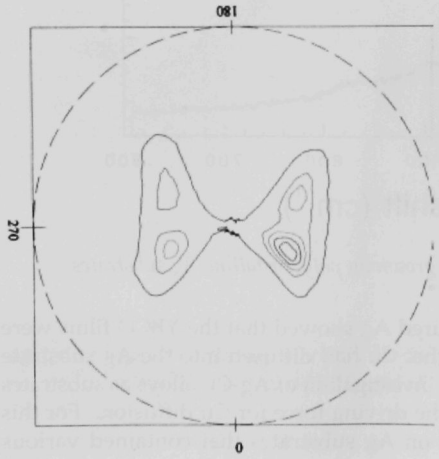

Fig. 29.
Ag(111) pole figure for Ag-0.20 at.% Cu substrate in the as-rolled condition.

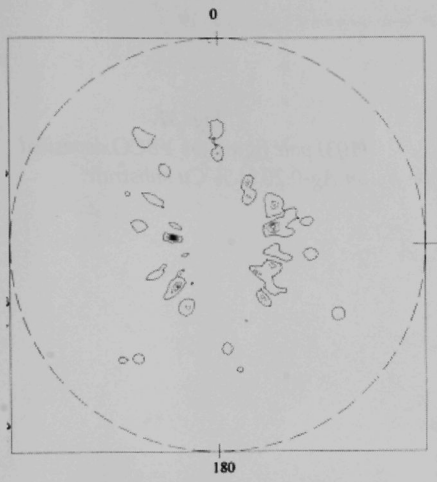

Fig. 30.
Ag(111) pole figure for Ag-0.25 at.% Cu substrate after being heated to the normal YBCO deposition temperature, then quenched.

to YBCO [7]. Indeed, a trace of YBCO in-plane alignment was found in all films deposited on Ag-Cu substrates (≥0.15 at.% Cu). The YBCO(103) pole figures showed four–fold symmetry for YBCO deposited on Ag-0.15 at.% Cu and Ag-0.2 at.% Cu (Fig. 31); YBCO deposited on Ag-0.25 at.% Cu presented eight-fold symmetry (Fig. 32), which indicates the coexistence of cube-on-cube and cube-on-diagonal orientations between YBCO and Ag. YBCO films deposited on pure Ag (9 ppm Cu), however, showed no in-plane epitaxy.

Raman studies revealed that YBCO films grown on Ag-Cu alloys (≥0.15 at.% Cu) are highly c-axis oriented (i.e., c-axis is normal to the substrate), whereas YBCO films deposited on pure Ag contain a mixture of a- and c-axis-oriented grains. This is shown in Fig. 33, where the average intensity ratio of the $I_{O(4)}/I_{O(2,3)}$ modes (used as a measure of out-of-plane texture of YBCO) is plotted against the Cu content in Ag. The O(4) mode, which results from a tilt of the c-axis with respect to the substrate normal, was very weak for samples with ≥0.15 at.% Cu. The O(4) mode was usually absent for YBCO films deposited on Ag-0.2 at.% Cu, indicating the best out-of-plane texture for these films. Also, the Raman results showed no evidence for barium cuprate or cation disorder in any of the YBCO films, independent of the Cu content in the Ag substrate.

The Cu content of the substrate also strongly influenced the superconducting properties of the YBCO films. Figures 34 and 35 show the superconducting transition onset temperature, T_c(onset), and the transition width, ΔT_c, for the YBCO films as functions of Cu content in the substrate. The T_c(onset) increased and the ΔT_c decreased as the Cu content increased to 0.2 at.% Cu; the substrate with this composition gave

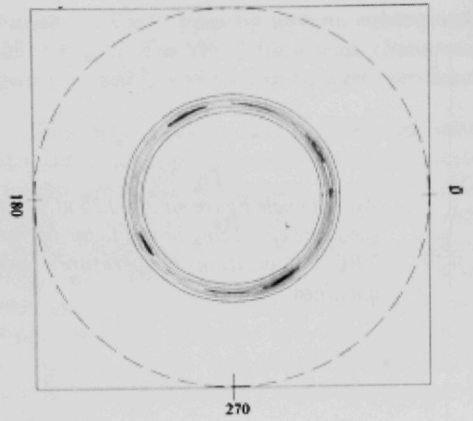

Fig. 31.
(103) pole figure for YBCO deposited on Ag-0.20 at.% Cu substrate.

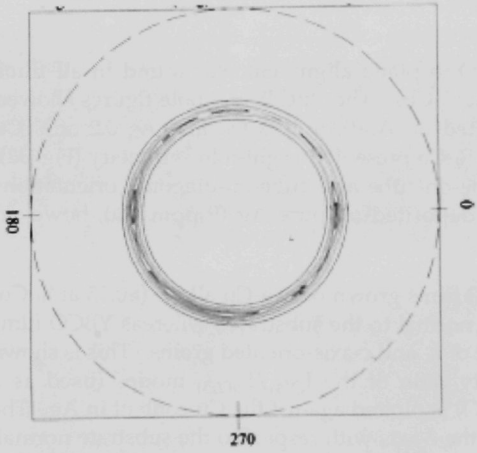

Fig. 32.
(103) pole figure of YBCO film deposited on Ag-0.25 at.% Cu.

YBCO with the highest T_c(onset), 91 K, and the smallest ΔT_c, 2K. As the Cu content increased beyond 0.2 at.% Cu, however, T_c(onset) decreased and ΔT_c increased. For comparison, T_c(onset) was ≈86 K for YBCO films deposited on pure Ag with ΔT_c ≈10 K. The inductive critical current, I_d, showed a similar, but sharper, trend with Cu content, as illustrated in Fig. 36. The highest I_d(>300 mA) was recorded for a YBCO film on Ag-0.2 at.% Cu.

These results show that the properties of YBCO films deposited directly on Ag substrates are significantly influenced by small concentrations of Cu in the substrate and that silver substrates with a Cu content of ≈0.20 at.% give the best superconducting

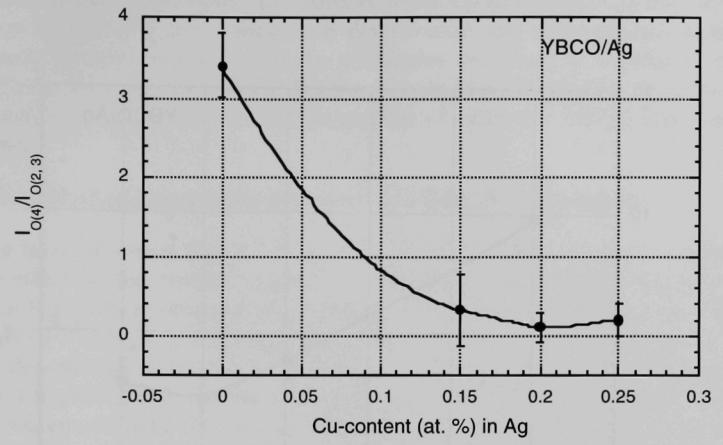

Fig. 33. Relationship between $I_{O(4)}/I_{O(2,3)}$, determined by Raman spectroscopy and used as a measure of out-of-plane texture of YBCO, and the Cu content of the Ag substrates.

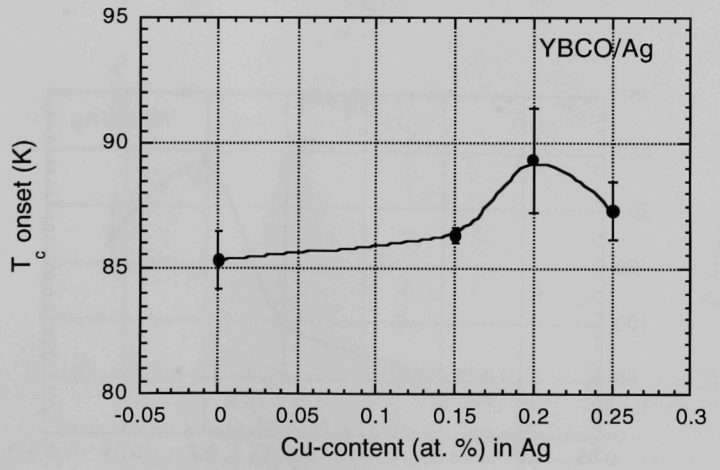

Fig. 34. Inductively measured T_c(onset) for YBCO films deposited directly on Ag vs. the Cu content of the Ag substrates.

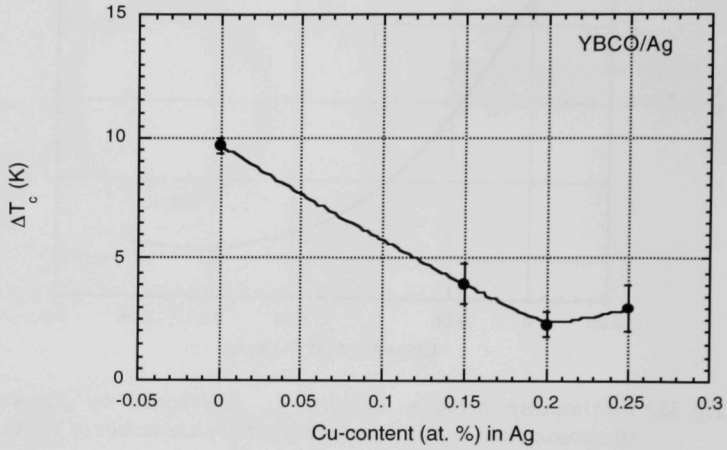

Fig. 35. Width of the superconducting transition, ΔT_c, for YBCO films deposited directly on Ag vs. the Cu content of the Ag substrates.

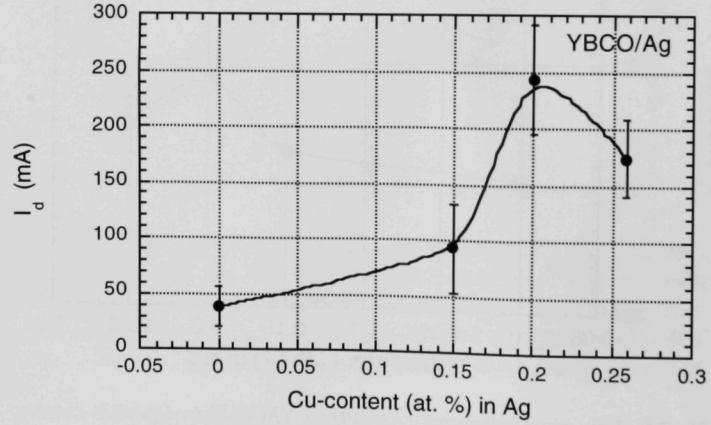

Fig. 36. Critical inductive driving current (I_d) for YBCO films deposited directly on Ag vs. composition of Ag substrate. Measurements were made at 70 K in self-field.

properties for the YBCO films. In addition, small Cu concentrations may influence the texture of silver substrates during their deformation and recrystallization; this may be important for obtaining textured Ag substrates on which it should be possible to deposit biaxially aligned YBCO. Further research is being done to understand the mechanism by which Cu affects the quality of both the YBCO films and the Ag substrates.

2.1.4 Effect of Magnetic History on Grain Boundary Transport

We have observed that the history in which the magnetic field is applied has a notable effect on the critical current of YBCO thin-film grain boundaries. The data shown in Fig. 37 were obtained from a single YBCO grain boundary, which we isolated in a RABiTS^{TM} sample (Oak Ridge National Laboratory). These results show additional history dependence beyond our earlier work. Previously, we showed that a sample exhibits a higher critical current when it is cooled to the measurement temperature in the measurement field (FC in Fig. 37) than when it is cooled to the measurement temperature in zero field before the measurement field is applied (ZFC in Fig. 37).

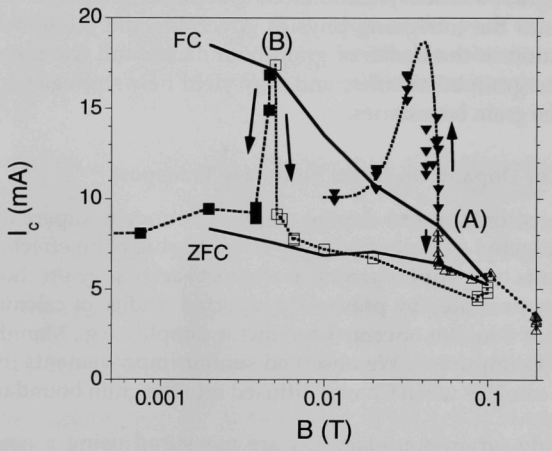

Fig. 37. History dependence of critical current of a YBCO grain boundary in a film grown by the RABiTS^{TM} process. Solid lines represent data obtained by field-cooling (FC) and zero-field-cooling (ZFC) to the measurement temperature (77 K). Triangles and squares represent field excursions after field-cooling to 0.05 T (point A) and 0.005 T (point B), respectively. Closed symbols show the effect of decreasing applied field on the critical current; open symbols show the effect of increasing field. The dashed lines are a guide to the eye only.

Our new results reveal that further enhancements can result from field excursions after the sample is field-cooled to the measurement temperature. The data indicate two distinct field regimes. After field-cooling in a modest (50 mT) magnetic field to the measurement temperature (point A in Fig. 37), a significant peak in the critical current data appears upon field reduction, whereas an increase in the field causes a monotonic reduction in the critical current. A similar peak effect was observed at Oak Ridge National Laboratory during field reduction from high fields (unpublished data). Near the peak position, the enhancement in critical current over field-cooled values is approximately a factor of two. In contrast, after field-cooling in a low field of several mT (point B in Fig. 37), the critical current drops sharply after either an increase or a decrease in the magnetic field.

The difference between the FC and ZFC measurements can be understood in terms of the different field histories that give rise to distinct flux profiles in the banks near the grain boundary. Apparently, these flux profiles strongly impact the pinning of grain boundary vortices and thus the grain boundary critical currents. This reinforces the importance of the interaction between grain boundary vortices and pinned vortices in the banks of the grain boundary. Similar consideration of the new data may provide further insight into the intriguing physics governing the relationship between the vortex configuration in the banks of grain boundaries and the potential for current transfer across the grain boundaries, and may yield new strategies for improving the performance of the grain boundaries.

2.1.5 Effect of Dopants on Grain Boundary Transport

The effect of strontium (Sr) doping on grain boundary supercurrent transport in YBCO was investigated as part of a larger effort to study the effects of various grain boundary dopants on supercurrent transport across grain boundaries. The investigation was stimulated by previously reported studies of calcium (Ca) doping in grain boundaries of thin film or coated conductor samples (e.g., Mannhart et al.), where J_c was significantly improved. We observed similar improvements in grain boundary transport in bulk samples when Ca was diffused into the grain boundaries.

For this study, grain-boundary J_c's are measured using a new technique that exploits SQUID measurements on ring samples. Well-controlled [001] tilt grain boundaries with desired misorientation angles are grown in bulk melt-textured YBCO using a dual seeding technique. Typical misorientation angles are ≈20°. This nondestructive technique and the use of bulk samples allow for extensive sample reprocessing so that diffusion and oxygenation effects can be systematically studied. It is likely that film samples are not sufficiently robust for such studies. Dopants and processing methods that improve the grain boundary J_c's of bulk YBCO rings are being investigated in coated conductor samples with the goal of minimizing energy losses across grain boundaries.

Our results indicate that Sr doping of grain boundaries does not appear to generally improve grain boundary transport, although improvement can apparently be achieved under certain processing conditions. Sr doping appears to significantly improve grain boundaries that have very low transport capability. With such grain boundaries, J_c was improved by a factor of five or more at 77 K. Even samples that initially gave no grain boundary transport showed a substantial J_c after Sr treatment (similar treatments with no Sr present showed no significant improvement). However, for bulk grain boundaries of high quality (i.e., those with J_c's in the upper range of values in the standard plots of J_c vs. misorientation angle), Sr treatment does not appear to be universally beneficial.

Most of our Sr diffusion studies were conducted with heat treatments at 970°C in the presence of $SrCO_3$. While Sr thoroughly decorates the grain boundaries, a complex aging process apparently occurs during the oxygenation step. Grain boundary oxygenation can be very rapid (even 2 h at 450°C in O_2 seems to oxygenate a grain boundary that extends across a 1 x 1 mm sample). For Sr-doped bicrystal rings, J_c is quite high after only a few hours of oxygenation, being comparable to untreated grain boundaries (i.e., those without Sr). After longer oxygen treatments, the J_c for Sr-doped bicrystals typically declines and saturates at 20 - 50% of the peak value. On the other hand, dense polycrystalline samples show, with remarkable robustness, a small (≈30%) improvement in J_c measured at 77 K, when given the Sr treatment and an extended (≈24 h) oxygenation.

The time evolution of J_c during the oxygenation of Sr-treated samples suggests that competing processes are at work, one process tending to increase J_c, while another decreases J_c. The characteristic times for these processes are different, each with its own temperature dependence. Preliminary studies indicate that J_c can be optimized by selecting the oxygenation conditions such that the positive process dominates. For example, we have observed that the J_c of a high-quality grain boundary without doping (maximum J_c obtained with a 450°C oxygenation) can be increased moderately (≈30 %) with a Sr treatment followed by oxygenation at low temperature (350°C).

These results suggest that the behavior of Sr in grain boundaries is highly complex. One possible cause for the complex behavior is that the YBCO phase decomposes during preparations at ambient pressure when the Sr concentration exceeds $x \approx 1$ in the system $YBa_{2-x}Sr_xCu_3O_{7-x}$ [8]. At the grain boundary interface, it is possible that the Sr concentration might be large enough that phase decomposition occurs, perhaps influenced by the level and kinetics of oxygenation. The results also suggest that optimized Sr diffusion and oxygenation treatments might lead to significant improvements in the grain boundary supercurrent transport. Similarly, optimized heat treatments with other dopants could also improve the grain boundary transport.

2.1.6 Diffraction Space Mapping of Coated Conductors

The growth of biaxially aligned films of $MBa_2Cu_3O_{7-x}$ (M-123, where M = yttrium or a rare earth element) on metal substrates relies on the texture of the substrate being transmitted to the M-123 film. The substrate can be a cube-textured metal (such as nickel or a nickel-base alloy) or a metal on which a cube-textured seed layer has been applied. The complete fabrication of coated conductor embodiments also requires a buffer layer to prevent the constituent metal atoms of the substrate from diffusing into the M-123 film. Hence, the architecture of an M-123 coated conductor typically consists of the metal substrate, a seed layer (if one is needed), a buffer layer, one or more cap layers (to enhance the epitaxy transmission), and the M-123 film. Whereas a relatively thick M-123 film is desirable (greater than a micron), most of the intervening layers (between the M-123 film and the metal substrate) range in thickness from 10 to 100 nm. The fabrication of this multi-layered epitaxial superstructure requires meticulous attention to detail at each stage of the process. Gaining a clear understanding of these details requires evaluation of the epitaxy and strain characteristics at each interface. This report summarizes recent work done at a third-generation synchrotron X-ray source using the technique of high-resolution DSM [9] to measure the texture, interplanar tilt, degree of orthorhombicity, and strain field pattern in M-123 coated conductor specimens.

The Eu-123 and Er-123 films on (100) $SrTiO_3$ (STO) single-crystal substrates reported on here were prepared by PLD from $EuBa_2Cu_3O_{7-x}$ and $ErBa_2Cu_3O_{7-x}$ targets [10]; they were provided by Q. Jia and S.R. Foltyn of the Los Alamos National Laboratory. Reported lattice parameters for the relevant materials are listed in Table 3. The DSM measurements were made at the Advanced Photon Source on the Materials Research Collaborative Access Team (MR-CAT) insertion device beamline (10-ID), which is equipped with an eight-circle Huber diffractometer. The diffraction patterns were recorded using an X-ray energy of 17 keV (0.72928 Å). The beam spot on the sample was slitted to a 2 mm by 1 mm rectangle. A Si(111) crystal analyzer was inserted between the sample and the detector to enhance the resolution.

Table 3. Lattice parameters for Eu-123, Er-123, and $SrTiO_3$ [11]

Material*	a (nm)	b (nm)	c (nm)
Eu-123^O	0.384	0.390	1.171
Eu-123^T	0.388	0.388	1.181
Er-123^O	0.382	0.389	1.169
Er-123^T	0.385	0.385	1.178
$SrTiO_3$	0.390	0.390	0.390

*The "O" and "T" superscripts refer to the orthorhombic and tetragonal structures, respectively.

High-resolution diffraction space maps were recorded for (1) an ≈160-nm-thick Eu-123 film on (100) STO, (2) an ≈160-nm-thick Eu-123 film on (100) STO that was precoated with ≈10 nm of Er-123, and (3) a clean (100) STO single-crystal specimen (to sort out substrate-related effects). The Eu-123/STO specimen showed no evidence of a T_c above 75 K, while the Eu-123/Er-123/STO specimen had a T_c of 92.5 K and exhibited a critical current density of 2.1 MA/cm^2. Diffraction space maps (2θ vs. ω) for the M-123-coated specimens are shown in Fig. 38. Included in Fig. 38 are maps for the diffraction space domains of (1) the (200) reflection of the STO substrate for the Eu-123/STO and Eu-123/Er-123/STO specimens, which also encompass the (006) reflection of the M-123 phases (Figs. 38a and 38b), (2) the (005) reflection of the M-123 phases (Figs. 38c and 38d), and (3) the (104)/(014) reflections of the M-123 phases (Figs. 38e and 38f).

The a- and b-axis lattice parameters for orthorhombic and tetragonal Eu-123 and Er-123 match the lattice constant of cubic STO (0.390 nm) within 0.01 nm, but their c-axis parameters are considerably larger (>1.1 nm). For this reason, M-123 films tend to grow cube-on-cube on (100) STO with the a-b planes parallel to, and the c-axis perpendicular to, the substrate surface. The measured lattice parameters for epitaxial M-123 films on textured substrates are primarily determined by two generally unrelated properties—oxygen content of the M-123 phase and interface characteristics that create strain. In the case of the Eu-123/STO specimen, the (006) reflection of Eu-123 appears at nearly the same 2θ value as the (200) reflection of STO (intense center spot in Fig. 38a) but at a slightly higher ω value (weak side spot in Fig. 38a). This is corroborated by the value of the (005) reflection in Fig. 38c, which equals the Eu-123 c-axis lattice parameter of 1.170 nm, i.e., exactly three times the STO lattice parameter and only 0.001 nm less than the c-value for unstrained, orthorhombic Eu-123 (Table 3). The small ω displacement of the Eu-123 (006) reflection is most probably due to a slight inter-planar tilt of the Eu-123 film relative to the STO surface.

In the case of the Eu-123/Er-123/STO specimen, the (006) reflection of the thin Er-123 film is presumed to fall on the (200) of STO in Fig. 38b since it also produces the weaker (005) spot near $2\theta = 17.94°$ in Fig. 38d; thus, it seems to match STO (200) in the same way the Eu-123 film does in the Eu-123/STO specimen. However, the Eu-123 film on top of the Er-123/STO substrate exhibits (006) and (005) reflections at lower 2θ values than does the Eu-123 on STO specimen (see Figs. 38a-d). The elucidation of this restructuring of the Eu-123 lattice in the presence of the Er-123 underlayer, as it relates to oxygen stoichiometry, cation disorder, and interfacial strain, is in progress.

Of greatest significance, however, are the differences in the (104)/(014) diffraction space maps for the two specimens (Figs. 38e and 38f). The Eu-123 film directly on STO appears to contain a single spot (Fig. 38e) indicating near equivalence of the (104) and (014) lattice diffraction spacings, and therefore, presumably, near equivalence of the

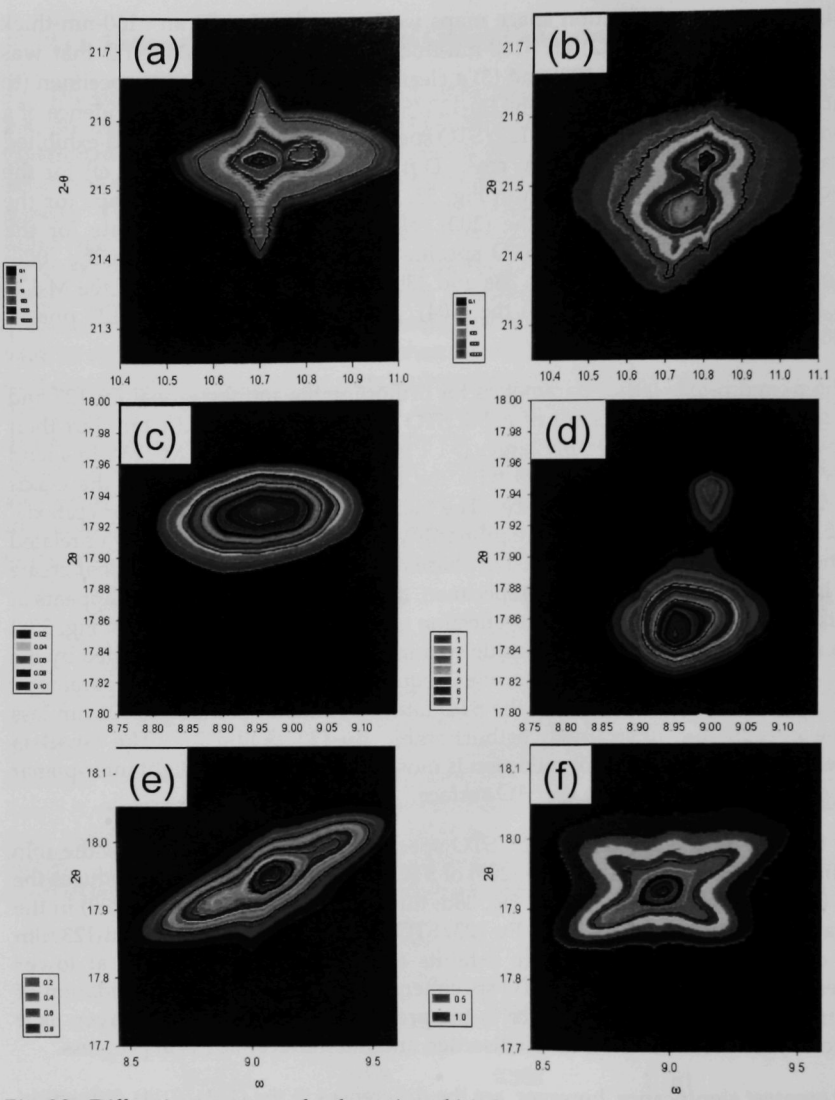

Fig. 38. Diffraction space map for the region of (a) the STO (200) and Eu-123 (006) reflections of the Eu-123/STO specimen, (b) the STO (200) and M-123 (006) reflections of the Eu-123/Er-123/STO specimen, (c) the Eu-123 (005) reflection of the Eu-123/STO specimen, (d) the M-123 (005) reflection of the Eu-123/Er-123/STO specimen, (e) the Eu-123 (104)/(014) reflections of the Eu-123/STO specimen, and (f) the M-123 (104)/(014) reflections of the Eu-123/Er-123/STO specimen. Intensity projections are logarithmic for (a) and (b) and linear for (c) through (f).

Eu-123 a and b lattice parameters. This finding is suggestive of a tetragonal lattice. Table 3 indicates that a tetragonal Eu-123 lattice would fit better on (100) STO than an orthorhombic one, because on average, a and b of Eu-123^T fit better on STO than do a and b of Eu-123^O. In the case of the Eu-123/STO sample, the oxygenation treatment given the sample should have produced orthorhombic Eu-123. Hence, we suspect that the STO substrate is forcing the Eu-123 into an oxygen-disordered structure. This condition might explain the absence of a T_c above 75 K. The diagonal streaking of the diffraction spot in Fig. 38e is attributable to a combination of strain field variation and elemental (cation and/or oxygen) disorder in the lattice [9]. The relative importance and magnitudes of these two phenomena are under investigation.

For the Eu-123/Er-123/STO specimen, we find two diagonally crossed spots in the Eu-123 (104)/(014) diffraction space map (Fig. 38f), suggesting that the Eu-123^O film in this specimen is twinned and influenced by strain and disorder as well. Seemingly, the thin Er-123 film does not transmit the straining influence of the (100) STO substrate to the Eu-123 film. Interestingly, the Eu-123 (006) and (005) diffraction space maps (Figs. 38a-d) exhibit a spreading in the ω-direction that indicates nanoscale misalignments in the Eu-123 mosaic [9]. Work in progress includes the correlation of diffraction space mapping results with T_c and critical current properties of M-123 coated conductors and the extraction of information about strain fields.

2.2 YBCO Bulk Conductors

2.2.1 YBCO Rings for Superconducting Shielded Core Reactors

Large YBCO ring and tube structures are being studied for possible use in a superconducting shielded core reactor (SSCR), a device that is under development as a fault-current limiter for power distribution grids. Intended for large-scale application, the design temperature is 77 K so low-cost refrigeration can be employed. Previous work includes the construction of a prototype Bi-Sr-Ca-Cu (BSCCO)-based device through a CRADA with the S&C Electric Company, an electrical switchgear manufacturer in Chicago [12]. Although the device functioned properly, various material-related limitations were discovered. A joint decision was reached to try substitution of oriented-grain YBCO rings in place of the BSCCO components.

Rings available from Superconducting Components Inc., of Columbus, Ohio, were tested for this application. Induced currents above 50 kA were achieved, and a simple fault-current limiter was demonstrated at that current level [13]. In the course of this work, transient magnetic field effects were studied by applying pulsed magnetic fields with rise times on the order of 10 ms. Because these devices are intended for use in a 60-Hz power distribution grid, a rise time of 4-5 ms is needed to duplicate the first quarter cycle of a 60 Hz sine wave under overload conditions. For faster measurements, various improvements were made to existing experimental equipment, as shown in Fig. 39.

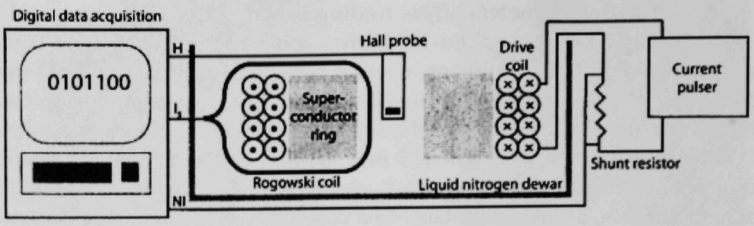

Fig. 39. Schematic diagram of experimental apparatus for testing of superconducting rings.

A copper-wire drive coil impresses a pulsed magnetic field on the outer surface of the superconducting ring that is being tested. The current pulser contains a large capacitor bank and custom-designed field effect transistor switch banks that allow short-duration current pulses to be manipulated. Current pulses of 500 A at 100 V, representing a power of 50 kW, can be readily controlled. Pulses up to about 150 kW can be achieved under more limited control. The data acquisition system can digitize multiple inputs at 16 bit accuracy with a cycle time of 200 μs. One of the inputs, marked "NI," records the voltage from a precision shunt placed in series with the drive coil. The shunt measures the drive current "I" as a function of time, but the drive coil has "N" turns (usually 60-600), so if the inductive coupling between the ring and drive coil is strong, the induced current will be "NI." A second input measures the voltage from a type of current transformer called a Rogowski coil. Changes in any current threading the coil produce a voltage in the coil through Faraday's Law, $V_{induced} = dI/dt$. Integrating this produces the value of the current threading the ring as a function of time. Because both the drive coil and superconducting ring thread the Rogowski coil, this variable is the sum of the two currents. The drive coil current is already known through measurement of the shunt and can be subtracted to produce the induced current in the superconducting ring, I_s. The magnetic field in the center of the ring is also recorded as a function of time.

The initial analysis was performed on a set of high-quality YBCO rings that were initially developed for a detailed analysis of the effects of grain boundaries on critical current, the control of which is a key problem in the development of successful SSCR devices [14]. The best of these rings had critical currents of about 20 kA/cm^2 at 77 K, a value that is appropriate for power grid applications. The size (typically 2.7 cm OD) and cross section (0.5 cm^2) are appropriate for testing, but are a factor of about four below the size needed for prototype development. The rings were highly uniform in their magnetic properties, a feature that was of considerable value in this study. Because the magnetic flux penetrates along radial directions around the entire circumference of the ring, variation of magnetic properties around the ring has the effect of averaging out millisecond-scale phenomena in each segment. Only when all the segments respond with similar flux dynamics can the millisecond-scale behavior of the structure be understood.

Figure 40 shows the behavior of one of the rings just before magnetic flux penetration. A pulse of 23 kA-turns was applied, with its magnitude peaking at 3 ms. The induced superconducting current I_s peaked at 9500 A. This is graphed as a negative current, because it is opposed in direction to the drive current, NI. The superconducting ring excluded much of the applied magnetic field from the center of the ring, but allowed the field to peak at about 5.5 ms. When the system was driven with a slightly larger pulse, 25 kA-turns, it approached the threshold of penetration, as shown in Fig. 41. Although the current functions hardly changed, the behavior of the magnetic field at the center of the ring shows the onset of penetration and temporal characteristics of magnetic diffusion. A further increase in the pulse to 27 kA-turns, shown in Fig. 42, produced a rapid and very uniform penetration in 3-4 ms. After this, a period of about 5 ms followed during which the induced current in the superconductor exhibited complex behavior and apparently reversed in direction. Explanation of the observed phenomena should lead to manipulation of the same and resultant performance improvements in SSCRs.

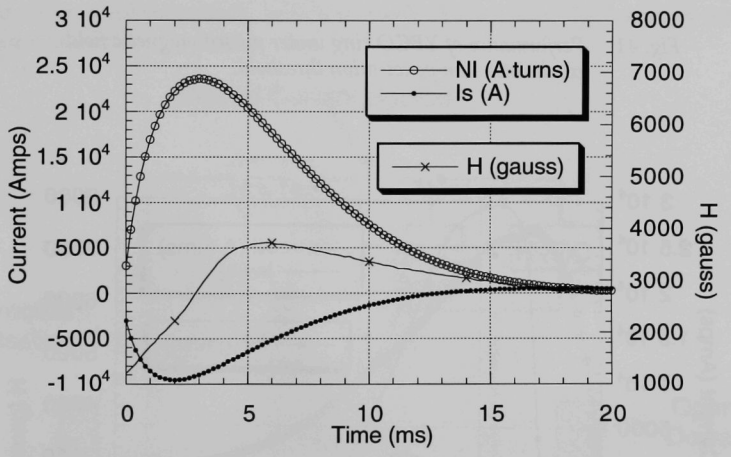

Fig. 40. Performance of YBCO ring under pulsed magnetic field conditions – approaching penetration.

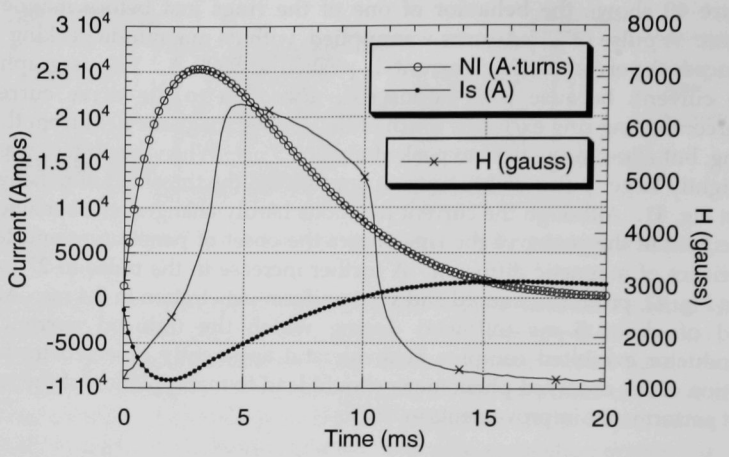

Fig. 41. Performance of YBCO ring under pulsed magnetic field conditions – on penetration threshold.

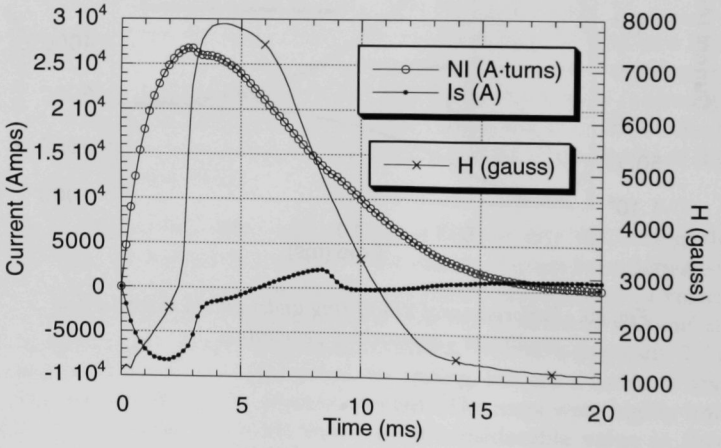

Fig. 42. Performance of YBCO ring under pulsed magnetic field conditions – after penetration.

2.2.2 Critical Current of YBCO Rings

Several melt-textured YBCO rings were received from Superconductive Components, Inc. (SCI). The dimensions of these rings were:

Minimum inside diameter = 1.60 in. (4.06 cm)

Maximum outside diameter = 2.77 in. (7.04 cm)

Average wall thickness = 0.38 in. (0.96 cm)

Average height = 1.29 in. (3.28 cm)

The rings were tested in pairs, and their critical currents were measured at the pulsed-current facility at ANL. Figure 43 shows a schematic diagram of the experimental apparatus, which consists of several capacitors in parallel and an array of field effect transistors (FETs). The capacitors are charged by a high-voltage DC current source (HVDC). The FETs are driven by a function generator, and the gates of the FETs can open and close in microseconds, which is much shorter than the transient time of the current experiments.

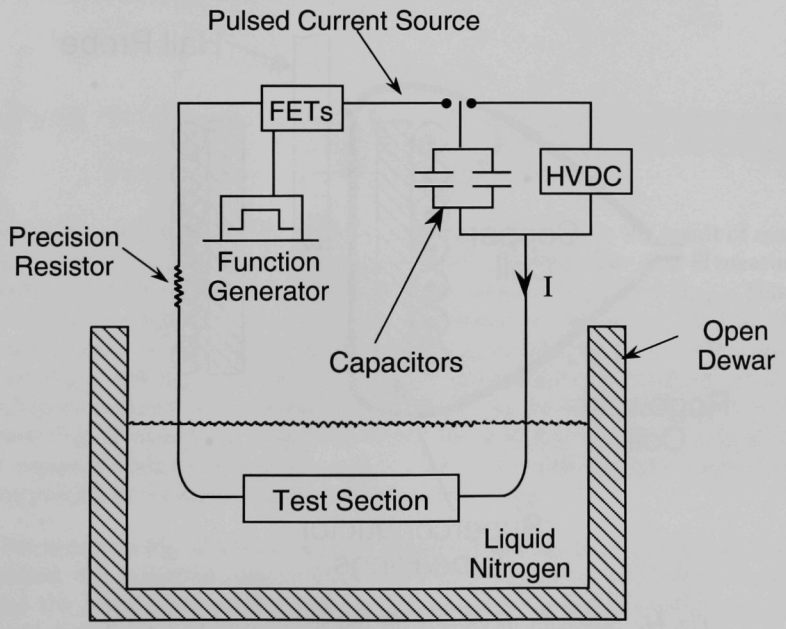

Fig. 43. Experimental apparatus for pulsed-current tests for measuring the critical currents of melt-textured YBCO rings.

Figure 44 shows a schematic diagram of the test section. A copper coil is wound on the outside of the superconductor ring pair. The copper coil has 200 turns and is connected electrically to the pulsed current supply shown in Fig. 43. A Hall probe is placed near the center of the superconductor ring pair to measure the magnetic field at the center of the rings. A Rogowski coil measures the induced current in the superconductor rings. The voltage output of the Rogowski coil is proportional to the rate of change of the current threading through the loop formed by the Rogowski coil. Integrating the voltage with respect to time yields the net current. The induced current in the superconductor tube is obtained by subtracting the net current from the current through the copper coil measured by the precision resistor. The entire test section is kept at 77 K by submersion in liquid nitrogen in an open dewar.

Figures 45 to 47 show typical test results. In these figures, N is the number of turns of the copper coil, I is the pulsed current in the copper coil, H is the magnetic field strength measured by the Hall probe, and I(ring) is the induced current in the superconductor ring pair, derived from the signal of the Rogowski coil. At relatively low excitation current (Fig. 45 with NI_{max} = 20,000 A-turns), the peak-induced current in the superconductor rings was 15,000 A and was in the opposite direction of

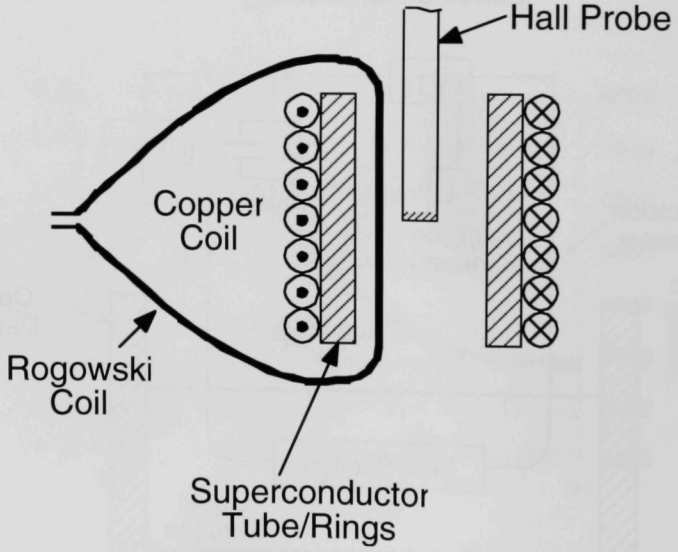

Fig. 44. Schematic diagram of the test section used to measure the critical currents of melt-textured YBCO rings.

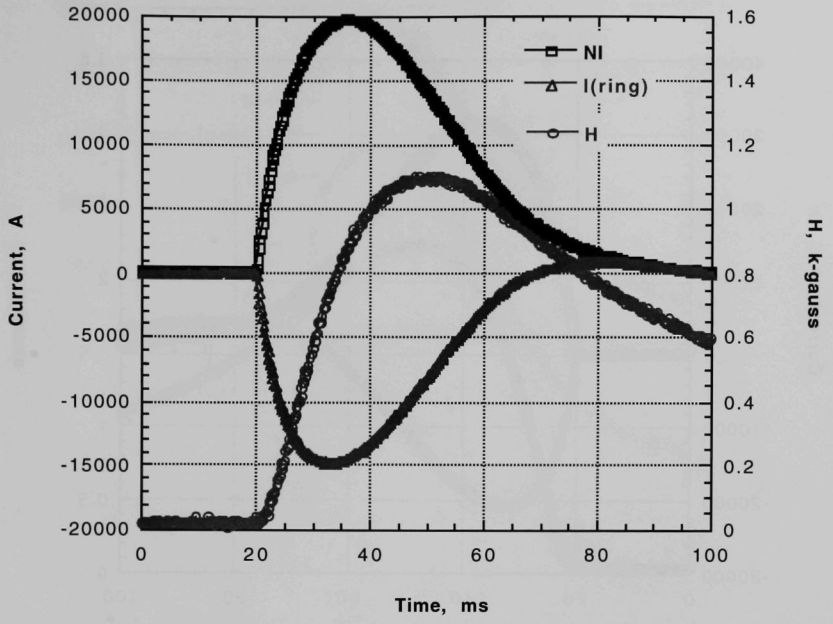

Fig. 45. Variations of the excitation current, NI, the magnetic field strength in the center of the YBCO rings, H, and the induced current in the YBCO rings, I(ring), versus time with NI_{max} = 20,000 A-turns.

the excitation current. The difference between NI and I(ring) is the result of magnetic flux leakage of the copper coil (not a long solenoid). The magnetic field H measured by the Hall probe shows a time delay of about 15 ms between NI_{max} and H_{max}. This delay is the result of magnetic diffusion, as is explained in references [15-17]. As the excitation current is increased (Fig. 46 with NI_{max} = 32,000 A-turns), the time delay between NI_{max} and H_{max} decreases to about 11 ms, and the maximum induced current in the superconductor rings increases to 20,500 A. As the excitation current is further increased (Fig. 47 with NI_{max} = 48,000 A-turns), the shielding capability (critical current) of the superconductor ring pair is reached, and the applied magnetic field penetrates the ring pair about 9 ms after the start of the current pulse.

The results in Fig. 47 exhibit several distinct characteristics. At the instant of field penetration, the excitation current NI decreases slightly with time before it rises again, because the impedance of the test section suddenly increases when the applied magnetic field penetrates the superconductor rings. At the same instant of field penetration, there is a slope change of the magnetic field H inside the superconductor

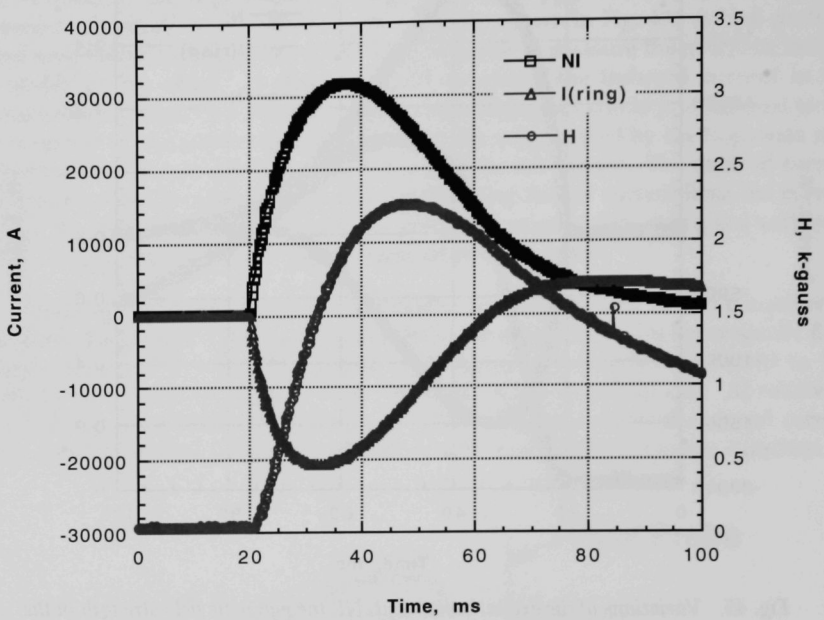

Fig. 46. Variations of the excitation current, NI, the magnetic field strength in the center of the YBCO rings, H, and the induced current in the YBCO rings, I(ring), versus time with NI_{max} = 32,000 A-turns.

rings. This occurs because the Hall probe is sensing the magnetic field generated directly, instead of through magnetic diffusion, from the current in the coil after the rings are penetrated magnetically by the applied field. Because the applied field has penetrated the superconductor rings, the delay between NI_{max} and H_{max} should disappear, as confirmed in Fig. 47. Finally, at the instant of field penetration, the induced current in the superconductor rings, I(ring), begins to drop sharply as a result of heat dissipation in the rings. The maximum induced current in the rings seems to level off just before the instant at field penetration. This stabilization indicates that the maximum in the induced current should correspond to the critical current of the rings.

From Fig. 47, the critical current of the ring pair is 26,000 A; therefore, the average critical current of one ring is 13,000 A. Note that the critical current measured here is the critical current under pulsed conditions, which is much higher than that under AC steady-state conditions. Under AC steady-state conditions, more heat is dissipated in the superconductor, and this heat loss reduces the critical current significantly.

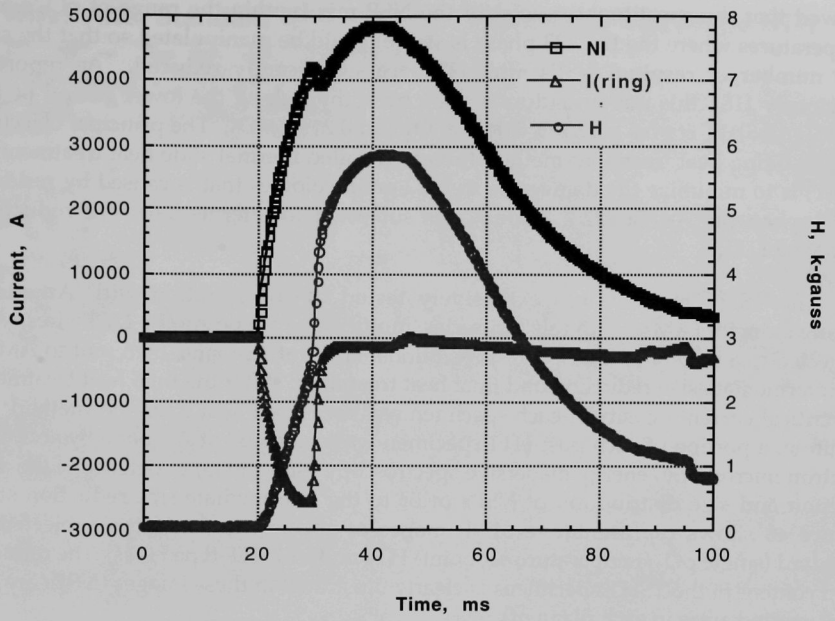

Fig. 47. Variations of the excitation current, NI, the magnetic field strength in the center of the YBCO rings, H, and the induced current in the YBCO rings, I(ring), versus time with NI_{max} *= 48,000 A-turns.*

2.3 Bi-Pb-Sr-Ca-Cu-O Conductors

2.3.1. Dissipation of Nonsuperconducting Second Phases (NSPs) in Multifilament Ag/Bi-2223 Composite Conductors

We previously presented results that showed how temperature and pO_2 influence phase evolution and microstructure development during the first heat treatment (HT1) of an Ag/Bi-2223 composite conductor fabricated by the powder-in-tube process. These results revealed that, for a given pO_2 in the range of pO_2's where the Bi-2223 phase is stable (nominally 0.04 to 0.21 atm), there is an onset temperature for the growth of robust Bi-2223 grain colonies (a desirable effect) and another onset temperature for the persistent formation of large NSPs (an undesirable effect). These two temperatures have been termed the grain-growth-takeoff temperature (GGTT) and the second-phase-takeoff temperature (SPTT), respectively. The results further showed that the composition of the NSPs varies significantly with pO_2 and temperature from a CuO-dominated mix at low pO_2 to a $(Ca,Sr)_2CuO_3$-dominated mix at intermediate pO_2 to a $(Ca,Sr)_{14}Cu_{24}O_{41}$-dominated mix at the highest pO_2. Based on these observations, we

showed that the constituent species of the NSP mix (within the range of pO_2's and temperatures where the Bi-2223 phase is stable) could be manipulated so that the size and number of residual NSPs after HT1 are significantly reduced. As reported previously [18], this manipulation is done by sliding along the lower bound of the GGTT and SPTT curves between 0.04 atm O_2 and 0.21 atm O_2. The principal objective of this sliding heat treatment method (hereafter called thermal slide heat treatment or TSHT) is to minimize the damage to Bi-2223 grain colonies that is caused by residual NSPs when the Ag/Bi-2223 conductor is subjected to intermediate size reduction following HT1.

The TSHT method was extensively tested in collaboration with American Superconductor (AMSC). In this test series, multifilament-type Ag/Bi-2223 wires were subjected to a variety of TSHT and conventional HT1's at Argonne, then sent to AMSC for intermediate size reduction and final heat treatment. After the final heat treatment, the critical current density of each specimen was measured by a transport method. In addition, a portion of each post-HT1 specimen was examined at Argonne by scanning electron microscopy/energy dispersive spectroscopy (SEM/EDS) to determine the area fraction and size distribution of NSPs prior to the intermediate-size reduction step. Figure 48 shows representative SEM images of specimens that were subjected to standard (single pO_2/temperature set point) HT1 and to TSHT-type HT1s. The reduced NSP content in the TSHT specimens is clearly illustrated in these images (NSPs are the dark spotted areas in each filament).

In Fig. 49 we show a plot that compares the area% of NSP after HT1 with the corresponding critical current density (J_c) in the fully processed state for a typical set of specimens from this study. A key result here is the precipitous increase in J_c for specimens with <8 area% NSP when compared to J_c for specimens with >13 area% NSP. This observation lends considerable support to the notion that at some level the NSPs remaining after HT1 can lead to a degradation of the J_c in fully heat-treated Ag/Bi-2223 wires. The data for specimens with <8 area% NSP must be examined to determine the extent to which other phase and microstructural characteristics of post-HT1 specimens have an influence on the J_c of fully processed wire.

2.3.2 Transmission X-ray Diffraction Measurements on Multifilament-type Ag/Bi-2223 Composite Conductor

The central step in the powder-in-tube process for Ag/Bi-2223 composite conductors is the heat treatment that transforms the ceramic powder mixture in the precursor billet into the superconducting Bi-2223 phase. Monitoring of this process as a function of process variables (e.g., time, temperature, and oxygen partial pressure) requires direct examination of the samples. The primary methods employed in virtually all cases today are X-ray diffraction (with a laboratory source) and SEM/EDS. With both of these methods, the sample must be sectioned and the silver

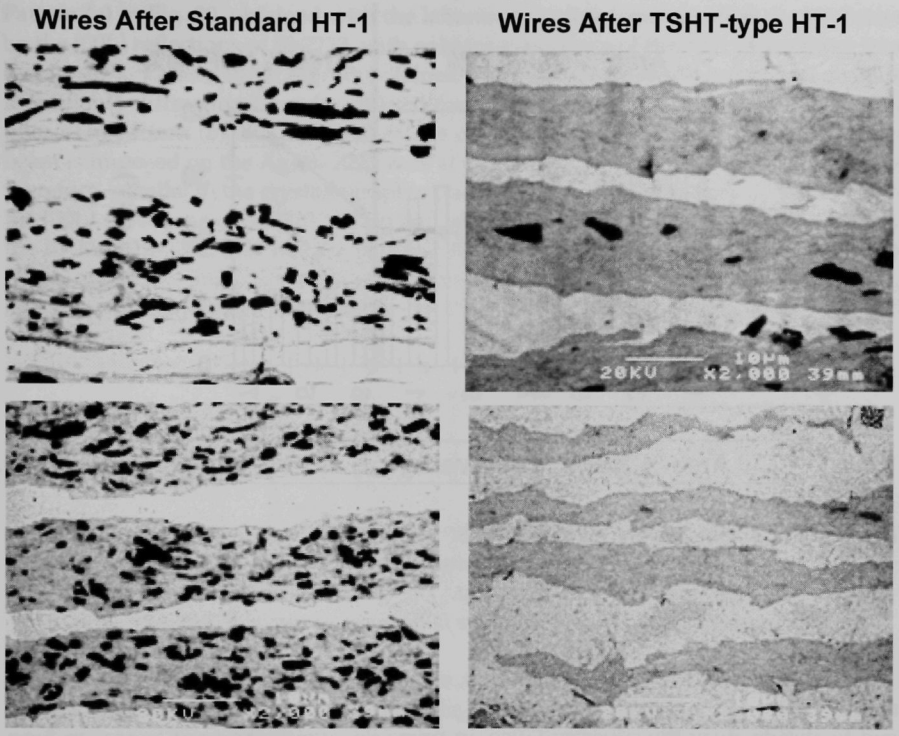

Fig. 48. Transverse section SEM images of representative Ag/Bi-2223 multifilament wire specimens after a standard (single pO_2/temperature set point) first heat treatment (left two images) and after an optimized TSHT-type first heat treatment (right two images). The dark spotted areas in the filaments are alkaline earth cuprate NSPs.

polished away to expose the superconducting ceramic cores, i.e., both methods involve destructive sectioning of the sample. In addition, during heat treatment of Ag/Bi-2223 composites, the Bi-2223 phase forms in a grain colony microstructure with the crystallographic c-axis perpendicular to the rolling direction. As a consequence of this texturing and the measurement configuration for the conventional theta/two-theta scan, the [00L] reflections of the layered cuprate phases (Bi-2212 and Bi-2223) dominate the diffraction pattern. Because of the dominance of the Bi-2212 and Bi-2223 peaks in the conventional X-ray diffraction (XRD) patterns, it is difficult to detect impurity phases, such as the 2201 phase, certain alkaline earth cuprates, and a lead-rich/copper-deficient cuprate known as the "3221" phase.

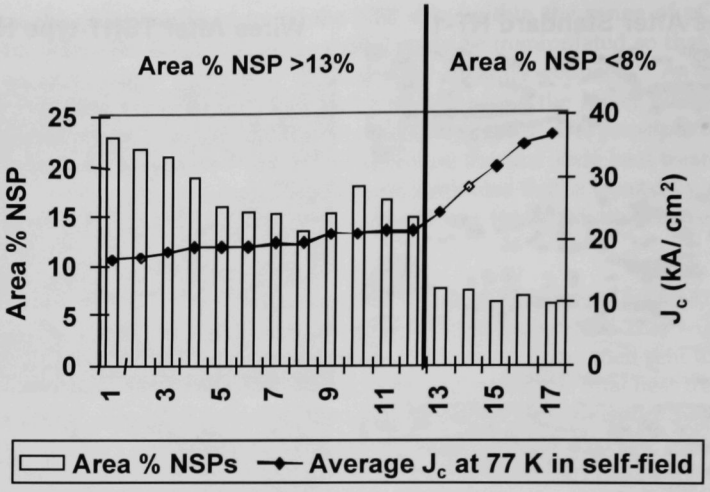

Fig. 49. Bar graph showing the area % NSP for post-first-heat-treatment Ag/Bi-2223 multifilament wire specimens subsequently subjected to intermediate size reduction and final heat treatment. The specimens are arranged in order of increasing J_c (from left to right) of the fully processed specimen.

As an alternative to conventional XRD, we investigated transmission XRD at X-ray energies high enough to fully penetrate the silver-sheathed composites. This avoids the need to abrade away the silver and also, in principle, avoids the need to section long lengths of composite wire. This method works very effectively at 25 keV (0.49594 Å), an energy that lies just below the silver Kα edge. Using this technique, we have determined the bulk second phase content of as-rolled, partially heat-treated, and fully heat-treated Ag/Bi-2223 specimens without any damage to the specimen itself. This allows us to investigate the same specimen at progressive stages of the deformation/heat treatment process.

The fully processed 51-filament Ag/Bi-2223 composite wires investigated in this study were provided by AMSC. The measurements were made on the MR-CAT insertion device beamline at the Advanced Photon Source using an eight-circle Huber diffractometer. The beam spot on the sample was slitted to a 2-mm by 1-mm rectangle. Patterns were recorded at ≈1°/min.

Figure 50 compares XRD scans for a typical Ag/Bi-2223 specimen that were obtained using the conventional/laboratory-source-based method (Cu-Kα) and the synchrotron-based transmission method. For comparison, the Cu-Kα data were recomputed to the 0.49594 Å wavelength used in the transmission experiment.

Pattern (a) in Fig. 50, obtained with the laboratory source/configuration, is dominated by the [00L] reflections of Bi-2223, with only trace evidence of the 3221 phase (near two-theta = 10°). Pattern (b) in Fig. 50, obtained using the transmission technique, contains identifiable diffraction lines for at least four other phases in addition to the Bi-2223 phase. In pattern (b), the [00L] reflections of Bi-2223 are not visible because the X-ray beam is imposed on the Ag/Bi-2223 wire at a right angle to the rolling direction and is, therefore, parallel to the crystallographic c-axis of the Bi-2223 grain colonies. Instead of the [00L] reflections of Bi-2223, the pattern contains mainly [10L] and [11L] reflections of the Bi-2223, Bi-2212, and Bi-2201 phases, plus at least four diffraction lines of the 3221 phase, and a low-angle reflection (≈4.3°) that may be due to either the $(Ca,Sr)_{14}Cu_{24}O_{41}$ alkaline earth cuprate or layered phase intergrowth boundaries. Also, the [200], [202],

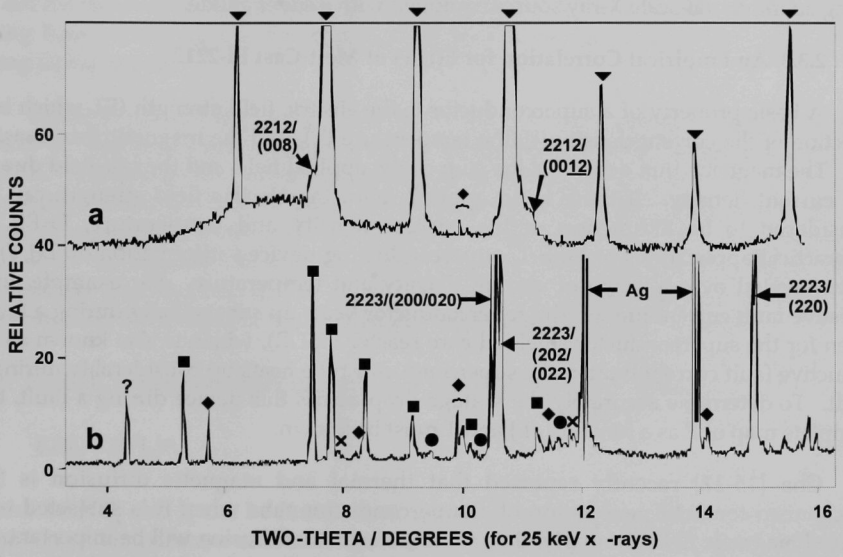

Fig. 50. Diffraction patterns from an abraded Ag/Bi-2223 composite wire. Pattern ***a*** *shows theta/two-theta diffraction pattern from an abraded Ag/Bi-2223 composite wire taken with a Cu-Kα laboratory source and recomputed to a wavelength of 0.49594 Å. Pattern* ***b*** *shows transmission-type two-theta of the same composite wire recorded using 0.49594 Å X-rays at the MR-CAT insertion device beamline. ▼ = [00L] of Bi-2223, ■ = [10L] and [11L] of Bi-2223, ✕ = [11L] of Bi-2212, ● = [11L] of Bi-2201, and ◆ = [HKL] of the 3221 phase. Beyond two-theta = 15°, the pattern consists of a near continuum of Bi-2223, Bi-2212, and Bi-2201 diffraction lines.*

and [220] reflections of Bi-2223 appear with considerable intensity, and like the two silver diffraction lines, they are actually off-scale in pattern **b** due to detector saturation. (Beam attenuation is required to bring the intensities of these two lines back into the dynamic range of the detector.)

Clearly, the 25 keV transmission XRD technique provides considerably more information about impurity phases in Ag/Bi-2223 composites than does the conventional laboratory-source-based method. This improvement is due, in large part, to the full transverse penetration of the Bi-2223 filaments achieved with the transmission method. Also, the absence of the Bi-2223 [00L] reflections in the transmission two-theta configuration is a testimony to the quality of the preferential Bi-2223 a-b plane alignment achieved by the powder-in-tube process. We are currently investigating the prospects for on-line transmission XRD of Ag/Bi-2223 composite wire using an industrial-scale X-ray source equipped with a silver anode.

2.3.3 An Empirical Correlation for E(J, T) of Melt-Cast Bi-2212

A basic property of a superconductor is the electric field strength (E), which is a function of the current density (J), the temperature (T), and the magnetic flux density (B). The magnetic flux density is the sum of the applied field and the self-field due to the current density. If there is no applied field, the electric field strength can be considered to be a function of the current density and temperature, E=E(J,T). In practical applications of high-T_c superconducting devices, information on E(J,T) is often needed over a range of current density and temperature. For example, in a resistive fault current limiter, the superconductor heats up substantially during a fault. Even for the superconductor shielded core reactor (SSCR), which is also known as an inductive fault current limiter, the superconductor tube heats up considerably during a fault. To determine accurately the voltage drop across this device during a fault, the complete map of E as a function of J and T must be known.

Cha [15-17] recently reported that thermal and magnetic diffusion is the mechanism for field penetration of a superconductor tube when it is subjected to a pulsed magnetic field. Similarly, thermal and magnetic diffusion will be important for the SSCR because it is based on the shielding capability of a superconductor tube. Furthermore, thermal and magnetic diffusion is also important for trapping of a magnetic field in a superconductor pellet using a pulsed current supply [19-21]. Modeling the coupled thermal and magnetic diffusion and understanding how the magnetic field and the temperature of the superconductor evolve during a transient require complete information on E(J,T), presumably from experimental measurement. However, such data are not widely available because most researchers only measure the E/J characteristics at one or two temperatures (mostly at 77 K).

In this report, we use the E/J data for a melt-cast Bi-2212 superconductor at two temperatures (77 and 87 K) to develop an empirical correlation for E(J,T) that can be

used to calculate E from 77 K to the critical temperature of 90-92 K. With this correlation, the electric field strength can be calculated for the range of temperature and current density that is relevant to the operation of practical devices made from melt-cast Bi-2212 superconductors. The correlation is based, in part, on the theory of magnetic relaxation [22], and the general form of the correlation may be applicable to other high-T_c superconductors.

The experimental data were reported previously [23]. The superconductor is a melt-cast Bi-2212 rod made by Hoechst (now called Nexans). The rod has a diameter of 7.85 mm. The standard four-point measurement technique was employed for all the tests with a distance of 87 mm between the voltage taps. The critical current was defined by the 1 μV/cm criterion. Braided current leads were soldered to the ends of the sample and connected to a pulsed power supply. A pulsed current with a duration of 400 ms (square wave) was used. The tests at 77 K were conducted in an open dewar using liquid nitrogen, and the tests at 87 K were conducted in the same open dewar using liquid argon.

Figure 51 shows the V/I characteristics of the melt-cast processed Bi-2212 rod at 77 and 87 K. The critical current defined at 77 K is one order of magnitude larger than that at 87 K. The tests were conducted by gradually increasing the current density and were terminated when the heating effect became appreciable. It should be noted that the range of experimental data for current density is relatively small at 87 K compared to that at 77 K, because the critical current density is much smaller at 87 K while dissipation and heating in the superconductor are much larger. Therefore, the experiment at 87 K had to be terminated at relatively small current density.

High-T_c superconductors usually obey the so-called power law,

$$E/E_c = (J/J_c)^n, \tag{1}$$

where both E_c and J_c can be functions of temperature, and the exponent n is a strong function of temperature and can vary widely for different high-T_c superconductors. The power law is the result of magnetic relaxation and can be explained in terms of the Anderson-Kim model for thermally activated flux creep [22],

$$E(J) = E_c \exp[-U(J)/kT], \tag{2}$$

If a logarithmic dependence of U on J is assumed,

$$U(J) = U_0 \ln(J_c/J), \tag{3}$$

then the result is the power law shown in Eq. 1 with

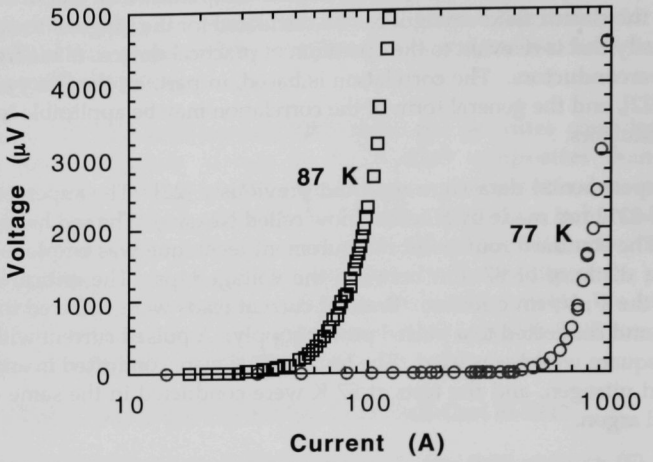

Fig. 51. Measured E/J characteristics at 77 and 87 K for a melt-cast processed Bi-2212 superconductor.

$$n = U_0/kT \,. \tag{4}$$

The parameter U_0 is independent of J but can be a function of T.

The theory of flux creep or magnetic relaxation is of little help in determining the temperature dependence of U_0. However, we know that the superconductor becomes an ohmic conductor when T approaches T_c, so the exponent n should approach one and the E/J relationship become linear. The following equation satisfies this condition,

$$n = U_0/kT = 1 + C_0 \ln(T_c/T) \tag{5}$$

where C_0 is a constant. It is easily shown that n=1 when $T=T_c$. From the experimental data at 77 and 87 K, $C_0 \cong 40$. Equation 1 can thus be written as

$$E(J,T) = f(T) \times J^n = f(T) \times J^{[1 + 40 \ln(T_c/T)]} \,, \tag{6}$$

where the function f depends only on temperature and is equal to

$$f(T) = E_c/(J_c)^n \,, \tag{7}$$

Employing the data in Fig. 51 to determine the constant coefficients (detailed development can be found in reference [24]), we obtained the final correlation for E(J,T):

$$E(J,T) = (39.236680 - 0.856427T + 0.004673T^2) \times 10^{2(T-89)} \times J^{[1 + 40 \ln(T_c/T)]}, \quad (8)$$

where T is the temperature in degrees Kelvin, the current density J is in A/cm^2, and the electrical field strength E is in $\mu V/cm$. Figure 52 shows the calculated E(J,T) values using Eq. 8 and the experimental data at 77 and 87 K. The correlation appears to match the experimental data at 77 and 87 K fairly well and is capable of predicting the general trend of E as a function of current density at other temperatures between 77 and 92 K. The correlation developed here is specifically for the melt-cast Bi-2212 superconductor because the coefficients were determined from the data in Fig. 51. The general form of E(J,T) given by Eqs. 2 to 7 may, however, be applicable to other bulk high-T_c superconductors, because it is based, in part, on the general theory of magnetic relaxation (thermally activated flux creep).

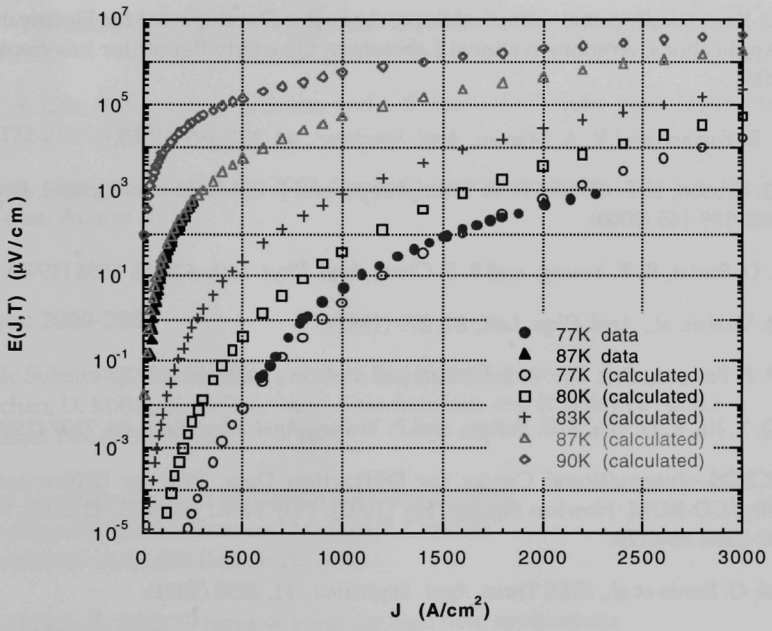

Fig. 52. Comparison of calculated E(J,T) with experimental data of a melt-cast Bi-2212 rod at 77 and 87 K.

References

1. U. Balachandran et al., Practical Superconductor Development for Electrical Power Applications, Argonne National Laboratory, Annual Report for FY 2001, ANL-02/03.

2. U. Balachandran et al., Practical Superconductor Development for Electrical Power Applications, Argonne National Laboratory, Quarterly Report for January-March, 2002.

3. B. Ma, M. Li, R. Koritala, B. L. Fisher, A. R. Markowitz, R. A. Erck, R. Baurceanu, S. E. Dorris, D. J. Miller, and U. Balachandran, submitted to *Superconductor Sci. and Tech.* (2002).

4. U. Balachandran et al., Practical Superconductor Development for Electrical Power Applications, Argonne National Laboratory, Quarterly Report for July-September, 2001.

5. J. R. Ferraro and V. A. Maroni, *Appl. Spectrosc.*, **44**, 351-366 (1990).

6. G. Gibson, L. F. Cohen, R. G. Humphreys, and J. L. MacManus-Driscol, *Physica C*, **333**, 139-145 (2000).

7. J. D. Budai, R. T. Young, and B. S. Chao, *Appl. Phys. Lett.*, **62**(15), 1836 (1993).

8. B. Veal et. al., *Appl. Phys. Lett.*, **51**, 279 (1987).

9. P. F. Fewster, *Crit. Rev. in Solid State and Mat. Sci.*, **22**(2), 69 (1997).

10. Q. X. Jia, X. D. Wu, S. R. Foltyn, and P. Tiwari, *Appl. Phys. Lett.*, **66**, 2197 (1995).

11. JCPDS—International Center for Diffraction Data, Powder Diffraction Data File/CD-ROM, Newton Square, PA (1993). PDF Nos.: 86-0473, 82-2303, 88-2254, 82-2308, 86-0179.

12. M. G. Ennis et al., *IEEE Trans. Appl. Supercond.*, **11**, 2050 (2001).

13. T. R. Askew and Y. S. Cha, *IEEE Trans. Appl. Supercond.*, **11**, 3947 (2001).

14. H. Claus et al., *Phys. Rev. B*, **64**, 144507 (2001).

15. Y. S. Cha and T. R. Askew, *Physica C*, **302**, 57-66 (1998).

16. Y. S. Cha, *Physica C*, **330**, 1-8 (2000).

17. Y. S. Cha, *Physica C*, **361**, 1-12 (2001).

18. U. Balachandran et al., Practical Superconductor Development for Electrical Power Applications, Argonne National Laboratory, Quarterly Report for January-March, 2000.

19. A. Terasaki, Y. Yanagi, Y. Itoh, M. Yoshikawa, T. Oka, H. Ikuta, and U. Mizutani, "Flux Motion during Pulsed-Field Magnetization in Melt-Processed YBCO," Advances in Superconductivity X, Proc. 10th Int. Symp. on Superconductivity 2, pp. 945-948, Gifu, Japan, October 27-30, 1997.

20. Y. Itol, Y. Yanagi, and U. Mizutani, *J. Appl. Phys.*, **82**(11), 5600-5611 (1997).

21. U. Mizutani, T. Oka, Y. Itol, Y. Yanagi, M. Yoshikawa, and H. Ikuta *Appl. Supercond.*, **6**(2-5), 235-246 (1998).

22. Y. Yeshurun, A. P. Malozemoff, and A Shaulov, *Rev. Mod. Phys.*, **68**(3), 911-949 (1996).

23. Y. S. Cha, S. Y. Seol, D. J. Evans, and J. R. Hull, *IEEE Trans. Appl. Supercond.*, **7**(2), 2122-2125 (1997).

24. Y. S. Cha, presented at the 2002 Applied Superconductivity Conference, Houston, Texas, August, 2002.

Patents: 2000-2002

Metallic Substrates for High-Temperature Superconductors
T. Truchan, D. Miller, K. C. Goretta, U. Balachandran, and R. Foley (U. of IL)
U.S. Patent No. 6,455,166 (Sept. 24, 2002)

Method for preparing high temperature superconductor
Uthamalingam Balachandran and Michael P. Chudzik
U.S. Patent No. 6,361,598 (March 26, 2002).

Shielded high-T_c BSCCO tapes or wires for high field applications
Uthamalingam Balachandran, Milan Lelovic, and Nicholas G. Eror
U.S. Patent No. 6,253,096 (June 26, 2001).

Thermomechanical means to improve critical current density of BSCCO tapes
Uthamalingam Balachandran, Roger B. Poeppel, Pradeep Haldar (IGC), and Lesizek Motowidlo (IGC)
U.S. Patent 6,240,619 (June 5, 2001).

Method of manufacturing a high temperature superconductor with improved transport properties
Uthamalingam Balachandran, Richard Siegel, and Thomas Askew
U.S. Patent No. 6,191,075 (February 20, 2001).

Bearing design for flywheel energy storage using high-Tc superconductors
John R. Hull and Thomas M. Mulcahy
U.S. Patent No. 6,153,958 (Nov. 28, 2000).

Method and apparatus for measuring gravitational acceleration utilizing a high temperature superconducting bearing
John R. Hull
U.S. Patent 6,079,267 (June 27, 2000).

Publications - FY 2002

Y. A. Jee, M. Li, B. Ma, V. A. Maroni, B. L. Fisher, and U. Balachandran, Comparison of Texture Development and Superconducting Properties of $YBa_2Cu_3O_x$ Thin Films Prepared by TFA and PLD Processes, Physica C, **356**/4, 297-303 (2001).

K. Salama (Texas Center for Superconductivity); S. P. Athur, and U. Balachandran, Texturing of REBCO Using Temperature Gradient, Physica C 357-360, 11-19 (2001).

J. R. Hull, Energy Storage Systems, Chapter 9.5 in "Properties, Processing, and Applications of YBCO and Related Materials," eds. W. Lo and A. M. Campbell, IEE Books, Stevenage, UK (2001).

J. R. Hull, Superconducting Bearings, Chapter 9.4 in "Properties, Processing, and Applications of YBCO and Related Materials," eds. W. Lo and A. M. Campbell, IEE Books, Stevenage, UK (2001).

M. Li, B. Ma, Y. A. Jee, B. L. Fisher, and U. Balachandran, Structural and Electrical Properties of Biaxially Textured $YBa_2Cu_3O_{7-x}$ Thin Films on Buffered Ni-Based Alloy Substrates, Mat. Res. Soc. Symp. Proc., Vol. 659, High-Temperature Superconductors -- Crystal Chemistry, Processing and Properties, pp. II10.2.1-2.6 (2001), eds. U. Balachandran, H. C. Freyhardt, T. Izumi, and D. C. Larbalestier.

Y. A. Jee, B. Ma, M. Li, B. L. Fisher, and U. Balachandran, Texture Formation and Superconducting Properties of $YBa_2Cu_3O_x$ Thin Films Prepared by Solution Process on $LaAlO_3$ Single Crystals, Mat. Res. Soc. Symp. Proc., Vol. 659, High-Temperature Superconductors -- Crystal Chemistry, Processing and Properties, pp. II9.17.1-17.6 (2001), eds. U. Balachandran, H. C. Freyhardt, T. Izumi, and D. C. Larbalestier.

T. M. Mulcahy, J. R. Hull, K. L. Uherka, R. A. Abboud, and J. Juna, Test Results of 2-kWh Flywheel Using Passive PM and HTS Bearings, IEEE Trans. on Applied Superconductivity, **11**(1), 1729-1732 (2001).

Y. S. Cha and T. R. Askew, Transient Characteristics of a High-T_c Superconductor Tube Subjected to Internal and External Magnetic Fields, IEEE Trans. on Applied Superconductivity, **11**(1), 2458-2488 (2001).

V. Selvamanickam, G. Carota, M. Funk, N. Vo, P. Haldar, U. Balachandran, M. Chudzik, P. Arendt, J. R. Grovesw, R. DePaula, and B. Newnam, High-Current Y-Ba-Cu-O-Coated Conductor Using Metal Organic Chemical-Vapor Deposition and Ion-Beam-Assisted Deposition, IEEE Trans. on Applied Superconductivity, **11**(1), 3379-3381 (2001).

T. R. Askew and Y. S. Cha, Transient Response of 50-KiloAmp YBCO Rings and Ring Pairs to Pulsed Magnetic Fields, IEEE Trans. on Applied Superconductivity, **11**(1), 3947-3950 (2001).

B. C. Prorok, J.-H. Park, K. C. Goretta, U. Balachandran; and M. M. McNallan (U. of Illinois at Chicago), Oxygen Diffusion Behavior During Internal Oxidation of Mg in Ag/1.12 at.% Mg, Physica C 370, 31-38 (2002).

B. Ma, M. Li, Y. A. Jee, R. E. Koritala, B. L. Fisher, and U. Balachandran, Inclined-Substrate Deposition of Biaxially Textured Magnesium Oxide Thin Films for YBCO Coated Conductors, Physica C 366, 270-276 (2002).

V. Vasanthamohan, T. B. Peterson, J. P. Singh, V. K. Vlasko-Vlasov, U. Welp, M. T. Lanagan, and G. W. Crabtree, Effect of Core Inhomogeneity on Strain Tolerance of Bi-2223 Composite Conductors, Supercond. Sci. Technol. 15, 94-98 (2002).

R. M. Baurceanu, V. A. Maroni, N. M. Merchant, A. K. Fischer, M. J. McNallan, and R. D. Parella, Investigation of a Multi-setpoint First Heat Treatment Methodology for the Silver-Sheathed $(Bi, Pb)_2Sr_2Ca_2Cu_3O_x$ Composite Conductor, Superconductor Science and Technology, 15, 1167-1175 (2002).

R. M. Baurceanu, V. A. Maroni, N. M. Merchant, A. K. Fischer, M. J. McNallan, and R. D. Parella, Time Evolution of Phase Composition and Microstructure in the Ag/Bi-2223 Composite Superconductor Heat-treated at Specific pO_2/Temperature Setpoints, Superconductor Science and Technology, 15, 1160-1166 (2002).

V. A. Maroni, K. Venkataraman, A. J. Kropf, C. U. Segre, Y. Huang, and G. N. Riley, Jr., Nondestructive Analysis of Phase Evolution and Microstructure Development in Ag/$(Bi,Pb)_2Sr_2Ca_2Cu_3O_x$ Composite Conductor by 25 keV Transmission X-ray Diffraction, Physica C, 382 , 21-26 (2002).

Y. L. Tang, D. J. Miller, R. M. Baurceanu, V. A. Maroni, and R. D. Parella, Improved Microstructure in Ag/Bi-2223 Composite Tapes by Systematic Variation of Heat Treatment Parameters, Superconductor Science and Technology, 15, 1365-1371 (2002).

U. Balachandran, B. Ma, M. Li, B. L. Fisher, R. E. Koritala, R. A. Erck, and S. E. Dorris, Inclined-Substrate Deposition of Biaxially Textured Template for Coated Conductors, Physica C, 378-381 , 950-954 (2002).

B. Ma, M. Li, B. L. Fisher, R. E. Koritala, and U. Balachandran, Inclined-Substrate Deposition of Biaxially Aligned Template Films for YBCO-Coated Conductors, Physica C 382, 38-42 (2002).

B. Ma, M. Li, R. E. Koritala, B. L. Fisher, S. E. Dorris, V. A. Maroni, D. J. Miller, and U. Balachandran, Direct Deposition of YBCO on Polished Ag Substrates by Pulsed Laser Deposition, Physica C, 377, 501-506 (2002).

M. Li, B. Ma, R. E. Koritala, B. L. Fisher, S. E. Dorris, V. A. Maroni, and U. Balachandran, Growth and Properties of YBCO Thin Films on Polycrystalline Ag Substrates by Inclined Substrate Laser Ablation, Superconductor Science and Technology, 15, 986-990 (2002).

B. Ma, M. Li, B. L. Fisher, and U. Balachandran, Ion-Beam-Assisted Deposition of Biaxially Aligned Yttria-Stabilized Zirconia Template Films on Metallic Substrates for YBCO-Coated Conductors, Superconductor Science and Technology, 15, 1083-1087 (2002).

Submitted

J. R. Hull, Flywheels, Contribution to the Encyclopedia of Energy, Elsevier Science, Academic Press, ed. C. Cleveland, 2003.

Distribution for ANL–03/3

Internal:

U. Balachandran
R. Baurceanu
Y. S. Cha
G. Crabtree
S. E. Dorris
H. Drucker
B. L. Fisher
K. C. Goretta
K. E. Gray
J. Harmon
J. R. Hull
J. Jorgensen
M. Kirk
S. Lake
M. Li
B. Ma
V. A. Maroni
D. J. Miller
J. J. Picciolo
R. B. Poeppel
A. C. Raptis
W. J. Shack
W. W. Schertz
J. P. Singh
A. M. Wolsky
TIS Files

External:

DOE–OSTI (2)
ANL–E Library
ANL–W Library

U.S. Department of Energy, Washington:

Office of Power Technologies, Energy Efficiency and Renewable Energy:
W. Parks
J. Daley
R. K. Dixon
R. George
M. Reed
H. Chhabra
Basic Energy Sciences–Materials Science:
T. J. Fitzsimmons
R. Gottschall
B. Strauss
A. Dragoo

Energy Technology Division Review Committee:
H. K. Birnbaum, University of Illinois at Urbana–Champaign
I.-Wei Chen, University of Pennsylvania
F. P. Ford, Rexford, NY
S. L. Rohde, The Peter Kiewit Institute
H. S. Rosenbaum, Fremont, CA
S. L. Sass, Cornell University
R. Zoughi, University of Missouri-Rolla

Other – Industry – University

S. Ahmed, Southern California Edison, Rosemead, CA
J. Badin, Energetics, Inc., Columbia, MD
P. Barnes, Air Force Research Laboratory, Wright-Patterson Air Force Base
P. Berdahl, E. O. Lawrence Berkeley National Laboratory
R. Bhattacharya, National Renewable Energy Laboratory
R. S. Bhattacharya, UES, Inc., Dayton, OH
R. W. Boom, University of Wisconsin – Madison
J. Bray, GE, Schenectady, NY
J. Cave, Hydro Quebec, Montreal, Canada
F. Chu, Ontario HydroTechnology, Toronto, Canada
P. Chu, University of Houston
J. Clem, Ames Laboratory
P. Clem, Sandia National Laboratories
C. Cox, Bob Lawrence and Associates, Inc., Alexandria, VA
A. Day, Boeing Corp., Seattle, WA
D. Driscoll, Rockwell Automation, Cleveland, OH
J. Ekin, National Institute of Standards and Technology, Boulder, CO
N. Eror, University of Pittsburgh
D. K. Finnemore, Ames Laboratory
A. Funkenbusch, 3M, St. Paul, MN
P. Grant, EPRI, Palo Alto, CA
D. Gubser, Naval Research Laboratory
P. Haldar, University at Albany, State University of New York
R. Hammond, Laboratory for Advanced Materials, Stanford University
R. A. Hawsey, Oak Ridge National Laboratory
P. Herz, TMS, Inc., Gaithersburg, MD
R. L. Hughey, Southwire Co., Carrollton, GA
Y. Iwasa, Francis Bitter National Magnet Lab., Massachusetts Institute of Technology
M. Justiniano, Energetics, Inc., Columbia, MD
M. Klein, University of Illinois at Urbana – Champaign
D. K. Kroeger, Oak Ridge National Laboratory
D. C. Larbalestier, University of Wisconsin – Madison
A. Lauder, DuPont, Wilmington, DE
M. Levine, E. O. Lawrence Berkeley National Laboratory
R. Loehman, Sandia National Laboratories
A. Malozemoff, American Superconductor Corp., Westborough, MA
F. Marciano, Pirelli Cables, Columbia, SC
K. Marken, Oxford Instruments, Inc., Carteret, NJ
B. McCallum, Ames Laboratory, Ames, IA
P. J. McGinn, University of Notre Dame
S. Mehta, Waukesha Electric Systems, Waukesha, WI
M. W. Morgan, Ability Engineering Technology, Inc., South Holland, IL
J. Muehlhauser, University of Tennessee
C. Oberly, Wright Air Force Laboratory, Dayton, OH
P. Pellegrino, IGC-SuperPower, Schenectady, NY

D. Peterson, Los Alamos National Laboratory
C. Rey, DuPont, Wilmington, DE
C. H. Rosner, CardioMag Imaging, Inc., Schenectady, NY
R. Russo, Lawrence Berkeley National Laboratory
H. Schneider-Muntan, National High Magnetic Field Laboratory, Tallahassee, FL
J. Schwartz, Florida State University
V. Selvamanickam, IGC-SuperPower, Schenectady, NY
G. Smith, PSC, Inc., Woodinville, WA
M. Strasik, Boeing Corp., Seattle
M. Suenaga, Brookhaven National Laboratory
H. Weinstock, Air Force Office of Scientific Research, Arlington, VA
D. O. Welch, Brookhaven National Laboratory
W. Wong-Ng, NIST
J. Worth, Oxford Instruments, Inc., Carteret, NJ